

Ultrahigh resolution topographic mapping of Mars with MRO HiRISE stereo images: Meter-scale slopes of candidate Phoenix landing sites

R. L. Kirk,¹ E. Howington-Kraus,¹ M. R. Rosiek,¹ J. A. Anderson,¹ B. A. Archinal,¹ K. J. Becker,¹ D. A. Cook,¹ D. M. Galuszka,¹ P. E. Geissler,¹ T. M. Hare,¹ I. M. Holmberg,¹ L. P. Keszthelyi,¹ B. L. Redding,¹ W. A. Delamere,² D. Gallagher,³ J. D. Chapel,⁴ E. M. Eliason,⁵ R. King,⁵ and A. S. McEwen⁵

Received 31 August 2007; revised 15 April 2008; accepted 21 July 2008; published 15 November 2008.

[1] The objectives of this paper are twofold: first, to report our estimates of the meter-to-decameter-scale topography and slopes of candidate landing sites for the Phoenix mission, based on analysis of Mars Global Surveyor (MGS) Mars Orbiter Camera (MOC) images with a typical pixel scale of 3 m and Mars Reconnaissance Orbiter (MRO) High Resolution Imaging Science Experiment (HiRISE) images at 0.3 m pixel⁻¹ and, second, to document in detail the geometric calibration, software, and procedures on which the photogrammetric analysis of HiRISE data is based. A combination of optical design modeling, laboratory observations, star images, and Mars images form the basis for software in the U.S. Geological Survey Integrated Software for Imagers and Spectrometers (ISIS) 3 system that corrects the images for a variety of distortions with single-pixel or subpixel accuracy. Corrected images are analyzed in the commercial photogrammetric software SOCET SET (® BAE Systems), yielding digital topographic models (DTMs) with a grid spacing of 1 m (3–4 pixels) that require minimal interactive editing. Photoclinometry yields DTMs with single-pixel grid spacing. Slopes from MOC and HiRISE are comparable throughout the latitude zone of interest and compare favorably with those where past missions have landed successfully; only the Mars Exploration Rover (MER) B site in Meridiani Planum is smoother. MOC results at multiple locations have root-mean-square (RMS) bidirectional slopes of 0.8–4.5° at baselines of 3–10 m. HiRISE stereopairs (one per final candidate site and one in the former site) yield 1.8–2.8° slopes at 1-m baseline. Slopes at 1 m from photoclinometry are also in the range 2–3° after correction for image blur. Slopes exceeding the 16° Phoenix safety limit are extremely rare.

Citation: Kirk, R. L., et al. (2008), Ultrahigh resolution topographic mapping of Mars with MRO HiRISE stereo images: Meter-scale slopes of candidate Phoenix landing sites, *J. Geophys. Res.*, 113, E00A24, doi:10.1029/2007JE003000.

1. Introduction

[2] Topographic modeling is an essential ingredient in selecting and certifying a safe and scientifically promising landing site for planetary surface exploration. Topographic obstacles at a variety of length scales can pose different hazards to successful landing; for example, landing radar systems can be “spoofed” by elevation changes over distances of hundreds of meters, causing the spacecraft to

execute the series of events needed for a safe landing at the wrong time and altitude. Whatever the other details of the entry, descent and landing (EDL) process, however, it is clear that steep slopes and topographic obstructions similar in size to the spacecraft itself (i.e., a few meters across or less) pose serious threats to any surface mission, such as mechanical damage caused by contact on landing, tipping over, or being unable to deploy moving parts fully. For this reason, topographic maps of potential landing sites with the highest possible resolution are always desired. The most detailed topographic information comes from stereo photogrammetric (and, to a lesser extent, photoclinometry or shape-from-shading) analysis of the highest-resolution images available. Over the last few generations of Mars surface missions, the resolution of this “best available” imagery has increased dramatically, by roughly 2 orders of magnitude. Premission mapping of the Mars Pathfinder landing site relied on Viking Orbiter images with a pixel

¹U.S. Geological Survey, Astrogeology Program, Flagstaff, Arizona, USA.

²Delamere Support Services, Boulder, Colorado, USA.

³CDM-Optics, Boulder, Colorado, USA.

⁴Lockheed Martin Space Systems, Denver, Colorado, USA.

⁵Lunar and Planetary Laboratory, University of Arizona, Tucson, Arizona, USA.

scale on the order of 40 m. Fortunately, an extensive sequence of images with stereo convergence from multiple angles was obtained in the 1970s, when the site was considered for the Viking landers. The analog stereoplotter technology available in the early 1990s was used to produce a relatively detailed contour map from these images, and a digital topographic model (DTM; the term digital elevation model or DEM is sometimes used interchangeably) was then generated by interpolating the contours [Howington-Kraus *et al.*, 1995] (the map appears in the work of Tanaka [1997]). The smallest details visible in a DTM of this type are typically dictated by the horizontal separation of the contours, which can be tens or hundreds of times larger than the grid spacing of the model. During the site selection process for the Mars Exploration rovers (MER), the narrow-angle Mars Orbiter Camera (MOC-NA) on the Mars Global Surveyor (MGS) spacecraft provided images and stereopairs with pixel scales as small as 1.5 m, though the most common operating mode was at 3 m pixel⁻¹. DTMs with an elevation measurement or “post” roughly every 3 pixels (i.e., 10 m in most cases) were produced directly from these images by fully digital or “softcopy” photogrammetric processing [Kirk *et al.*, 2003b]. MOC stereo images were also the best source of topographic information in the early phases of the landing site selection process for the Phoenix mission, as reported in section 2 [Kirk *et al.*, 2006b]. Late in 2006, however, the High Resolution Imaging Science Experiment (HiRISE) onboard the Mars Reconnaissance Orbiter (MRO) began to provide images at a pixel scale near 0.3 m from which 1 m post⁻¹ DTMs could be generated. The sheer size of HiRISE images (often exceeding 1600 megapixels [McEwen *et al.*, 2007]) means that stereo mapping could not even be contemplated without digital techniques, and that efficiency depends on automating as much of the procedure as possible.

[3] Our objectives in this paper are twofold. First, we describe our topographic mapping of candidate Phoenix landing sites with both MOC and HiRISE images and discuss the implications of the results for a safe landing. Second, we document here in detail for the first time the geometric calibration and photogrammetric processing of the HiRISE images that make meter-scale topographic mapping of Mars possible. Where we can, we compare the HiRISE DTMs with other topographic data in order to validate our methods and results, but we note that this is quite challenging because, with the exception of lander and rover panoramic imagery, no other data sets approach let alone surpass the resolution of HiRISE. HiRISE targeting plans include obtaining several hundred to a thousand stereopairs during the two-Earth-year prime mission. These pairs, and the tools needed to produce quantitative topographic information from them, will be a tremendously valuable resource for all branches of Mars science as well as for mission planning and operations in the years to come.

2. Landing Site Selection and MOC Mapping

2.1. Landing Site Selection Criteria

[4] The Phoenix Lander is designed to touch down on the high northern latitudes of Mars, characterize the surface, acquire and analyze samples of soil and ice, and monitor atmospheric conditions [Smith *et al.*, 2004, 2006, 2008].

Candidate landing sites are restricted to the zone from 65–72°N latitude, bounded on the south by the scientific requirement for accessibility of ground ice at relatively shallow depths and on the north by the engineering criterion of adequate solar power. Within this zone, several 20° × 7° regions designated by letters A through E were selected at an early stage for intensive characterization and possible targeting, based primarily on initial estimates of subsurface ice abundance [Boynton *et al.*, 2006; Mellon *et al.*, 2008]. Longitude ranges for the selected regions are A, 250–270°E; B, 120–140°E; C, 65–85°E; and D, 230–250°E. Among the engineering requirements for a safe landing site are a rock abundance (cumulative area fraction) ≤18% based on the established rock population at the Viking Lander 2 site and slopes less than 16° over all horizontal baselines greater than 1 m [Arvidson *et al.*, 2006, 2008]. These requirements are, strictly speaking, rules of thumb; the final assessment of site safety was based on obtaining an acceptable failure rate in Monte Carlo simulations of the EDL process that incorporate observed rock populations and DTMs [Guinn *et al.*, 2006]. The upper limits on rock abundance and slope are useful, however, because they can be used in preliminary screening to eliminate unacceptable candidates. This screening can be done by working from the lowest-resolution data sets such as Mars Orbiter Laser Altimeter (MOLA) topography [Smith *et al.*, 2001] for slopes over the longest baselines, though the intermediate-resolution MOC data set to HiRISE. Higher-resolution data may reveal more rocks or greater slopes than were suspected at low resolution, but they will never reveal fewer such hazards than already seen and therefore cannot lead to a hazardous site being reclassified as safe. Thus, the MOC image data set was the main focus of both rock counting and of our topographic mapping until late in the selection process when HiRISE became available.

[5] The geomorphologic diversity of the candidate landing sites for Phoenix is considerably less than that of the sites considered for MER [Seelos *et al.*, 2006, 2008]. Similar kilometer-scale features are seen in the lettered regions, throughout the zone that contains them and, indeed, over a somewhat wider range of latitudes. These include systems of ridges tens of kilometers apart and hundreds of kilometers in length (Panchaia Rupes); hills and knobs (including but not limited to Scandia Colles); kilometer-scale polygons and other types of patterned ground; pedestal craters with ejecta and interiors elevated above the surrounding plains; and a small number of relatively fresh impact craters. These classes of features are resolved by MOLA altimetry, which indicates that the deepest craters measure no more than 300 m from floor to rim and that the local relief of other features is 100 m. Superimposed on all these features is patterning at scales of a few tens of meters. Depending on the planform and the relative prominence of high regions versus the network of lows surrounding them, this decameter patterning may be described as “polygonal,” “fingerprint,” or “basketball” terrain in different areas. Albedo variations, mostly correlated with topography, are ubiquitous and have considerable impact on the photoclinometric (PC) analysis. Such variations include diffuse, low-albedo regions associated with hills, crater rims, and other high areas and locally higher albedo in the troughs of the decameter-patterned ground than on its protuberances. Seasonal variations in

Table 1. MOC Image Sets Mapped for Candidate Phoenix Landing Sites and Analogs^a

Site	E Lon (°)	Lat (°)	Image 1	Image 2	Res 1 (m)	Emiss ang 1 (°)	Res 2 (m)	Emiss ang 2 (°)	RMS Slope (°)	Baseline (m)	Description
VL2	134.1	47.7	M18-01458	E18-01397	1.81	0.11	1.87	17.96	4.14	6	ST SE of Viking landing site
PHX 0	196.8	73.1	E02-01891	R01-01314	3.02	0.36	3.39	22.95	4.54	1.8	PC hilly subarea
PHX A1	251.9	66.6	M23-02019	E23-00945	7.31	0.19	5.18	18.10	0.45	115	MO kilometer-scale polygons
PHX A2	258.7	68.7	R22-01155	R23-00902	3.36	18.10	4.33	31.31	0.82	3	PC
PHX B1	130.4	67.5	R22-00168	S01-00644	3.35	18.16	3.35	18.09	1.55	5.2	PC
PHX B2	131.6	67.4	R22-00846	R23-00231	3.36	18.09	4.23	30.02	0.83	12	ST subdued crater
PHX B3	131.4	67.0	S01-00601	S02-00705	3.36	18.11	6.36	30.20	1.78	10	ST subdued crater
PHX B4	126.6	66.8	S01-00875	S02-00736	3.36	18.09	4.56	33.62	2.48	10	ST hills
PHX B5	124.4	67.6	R20-01522		8.42	18.27			1.57	10	ST hills
PHX B6	132.7	67.8	R23-00188	R21-00441	3.37	18.22	3.36	18.13	1.04	10	ST hills
PHX B7	132.7	67.7	R22-01248		3.37	18.14			1.33	7.1	PC fresh crater ejecta
PHX C1	64.9	69.4	M19-01733	E19-00409	5.99	0.38	6.13	18.18	1.54	3.1	PC pedestal crater, ratio image
PHX D1	118.6	68.1	M00-00483	R19-02207	1.82	0.15			0.86	5.8	PC ridge, subdued crater
									1.46	18	ST subdued crater ejecta
									4.40	6	ST subdued crater

^aMOC, Mars Orbiter Camera; Res, Resolution in m pixel⁻¹ across track; Emiss ang, emission angle; root-mean-square (RMS) slope, bidirectional root mean squared slope over given baseline; ST, stereo; PC, photoclinometry.

albedo can also interfere with matching of images for stereoanalysis. The similarity of decameter- and kilometer-sized features over much of the northern lowlands is fortunate, because it reduces the number of distinct geomorphic and, in particular, hazard units [Barge and Parker, 2006] whose topographic properties must be characterized, and thus reduces the volume of image data required.

2.2. MOC Image Data

[6] Atmospheric conditions only permit imaging of the surface in the Phoenix latitude zone for a portion of each Mars year [Liu *et al.*, 2003]; this season is shorter for MOC than for HiRISE, which is designed to have higher signal-to-noise ratio (SNR). The last such period prior to 2006 was from August 2004 to January 2005; we believe we have identified and analyzed all useful MOC stereopairs and single images of the candidate Phoenix landing sites that were obtained through this time. Prior to the start of the Phoenix site selection process, the density of MOC images was lower at the latitudes of interest than elsewhere on Mars, and our database of validated stereopairs [Kirk *et al.*, 2004] contained only three pairs within the lettered regions. These are listed as Phoenix A1, C1, and D1 in Table 1. Useful pairs covering somewhat similar terrain were also found at the Viking 2 landing site (VL2) south of the Phoenix zone [Kirk *et al.*, 2004] and the site listed as Phoenix 0 to the north. This dearth of stereopairs is undoubtedly a direct result of the homogeneity of the northern plains. Fortunately, many of the images in this region, including most of those forming stereopairs, were targeted to impact craters. Local relief on these craters is generally the best available information for calibrating PC against the stereo results.

[7] In support of the Phoenix site selection process, the MOC team targeted the lettered regions extensively during the period of relative atmospheric clarity from August 2004 through January 2005. Five additional stereopairs, designated Phoenix A2 and B1–B4, were obtained in this campaign and analyzed by us. Unfortunately, albedo variations in all these models (and also in C1 and D1) were so severe as to prevent us from obtaining useful results by PC. In general, decameter-scale albedo variations in the plains

were noticeable but not severe; these would act to introduce spurious slopes into the photoclinometric DTMs, but because the resulting slope distributions would systematically overestimate the true hazards, they might still have been useful for the hazard analysis. The kilometer-scale diffuse dark areas associated with topographic highs posed a more serious problem, however. By overwhelming the contrast of topographic shading, these dark areas prevented us from using the stereo-derived topography of these features to obtain atmospheric haze estimates and thus to calibrate the results of PC. Uncalibrated, our slope estimates could easily be in error by a factor of 2 or more, rendering them much less useful for assessing the safety of sites at which true roughness begins to approach the maximum acceptable level.

[8] Additional topographic and slope results reported here were obtained by adopting a novel strategy to calibrate MOC images for photoclinometry. In the course of preparing base mosaics for hazard mapping, Barge and Parker [2006] had examined all available MOC images in the candidate sites and registered all of those containing identifiable features to the MOLA global DTM known as the Mission Experiment Gridded Data Record (MEGDR, available at <http://pds-geosciences.wustl.edu/missions/mgs/megdr.html>). This yielded a new and larger pool of candidate images not in stereopairs for which a priori topographic information was available. Of nine features in region B with promising MOLA relief for calibration and MOC image coverage, six were eliminated from our processing efforts because of albedo variations or other problems. The remaining sites, Phoenix B5–B7, were analyzed to produce photoclinometric DTMs calibrated to MOLA. The B6 data set is noteworthy because two overlapping images were available, with similar viewing angles (i.e., not providing useful stereo) but with illumination from opposite sides (Figure 1). We were able to register these images and form a ratio image from which albedo variations were largely eliminated. Such processing of visible-band images with differing illumination to eliminate albedo is a variant on the “magic airbrush” processing we have previously described for synthetic aperture radar data [Kirk, 1993] and for Thermal Emission Imaging Spectrometer (THEMIS) VIS + IR data [Kirk *et al.*, 2005]. The application to MOC relies on images with

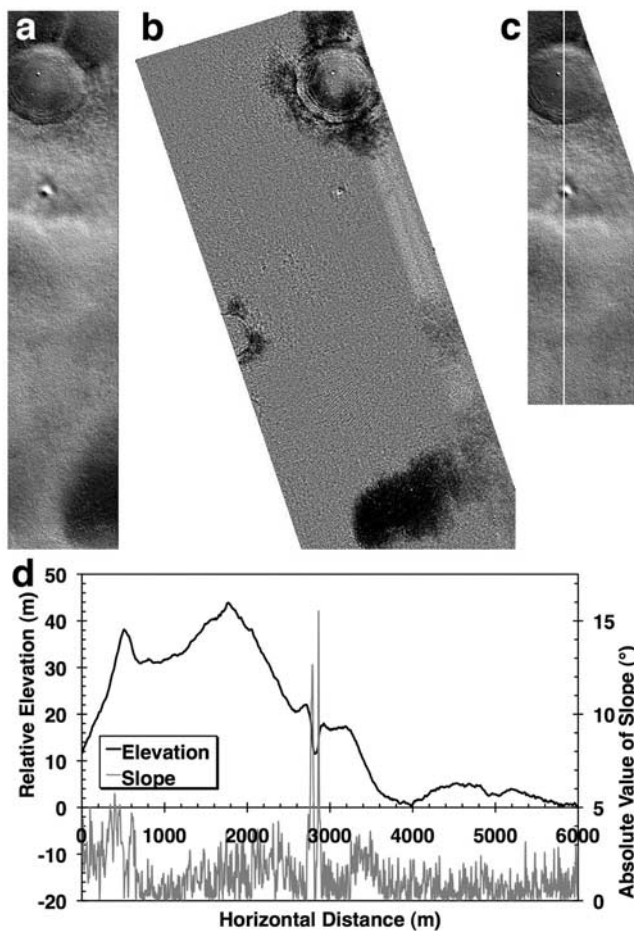


Figure 1. Combination of Mars Orbiter Camera (MOC) images for site PHX B6 to reduce impact of surface albedo variations on topographic and slope estimates from photoclino-metry. (a) Portion of MOC image R23-00188, illuminated from lower left with incidence angle 82.3° . (b) Portion of MOC image R21-00441, map projected to register to Figure 1a. Illumination is from upper right with incidence angle 47.0° , so topographic shading is weaker and reversed, while albedo variations are relatively emphasized. (c) Ratio of image in Figure 1a to that in Figure 1b, after subtracting an appropriate atmospheric haze contribution from each. Surface albedo variations have almost entirely canceled, making this “magic airbrush” image combination suitable for photoclino-metry. Poorly calibrated columns of data along the edge of R21-00441 have been excluded from the analysis, as has the bottom portion of the overlap area, where the dark albedo pattern has changed shape between the two observations. (d) Elevation and slope profiles along the column marked in Figure 1c. Slopes in the small pit crater exceed 10° but those elsewhere, including the qualitatively dramatic pedestal crater, are on the order of 3° or less, over baselines of 3.13 m.

different illumination directions (similar to the radar case; THEMIS processing is instead based on comparing reflected and absorbed/reemitted radiation), but resembles the THEMIS case in that an appropriate haze contribution must be subtracted from one of the images in order for the albedo variations to be canceled. This haze correction was deter-

mined empirically. Undercorrection leaves the original albedo variations (dark patches) partly visible, whereas overcorrection results in reversal of the apparent feature contrast, resulting in bright patches. Thus, the present result is somewhat subjective and only reduces the albedo variations to the extent that the human eye is sensitive to such patterns. In principle, however, it would be possible to automate the procedure by determining an objective measure of the presence and strength of albedo variations. We also note that images with opposite-side illumination provide the strongest separation of shading from albedo variations. If one used images with same-side illumination, the topographic shading would partially cancel in the image ratio that eliminates albedo variations. Such images could nevertheless be used if the incidence angles were sufficiently different.

2.3. Methodology

[9] The techniques we use for deriving topographic data from MOC images by stereoanalysis and photoclino-metry are described in detail by Kirk *et al.* [2003b]. They are the same for Phoenix site mapping as for MER and also form the basis for the slightly modified processing of HIRISE images described in section 3. We use the USGS in-house digital cartographic software ISIS 2 [Eliason, 1997; Gaddis *et al.*, 1997; Torson and Becker, 1997] for mission-specific data ingestion and calibration, as well as “2-D” processing such as map projection, image mosaicking, and photoclino-metry [Kirk, 1987; Kirk *et al.*, 2003a]. Slope analysis is also performed with (unreleased) software that reads ISIS image files. Our commercial digital photogrammetric workstation running SOCET SET ([®] BAE Systems) software [Miller and Walker, 1993; 1995; Zhang and Miller, 1997] is used for “3-D” processing steps such as control of the images and automatic extraction and manual editing of DTMs. SOCET SET includes a pushbroom scanner sensor model that is physically rigorous but “generic” enough (in the sense of allowing instrument parameters such as focal length and detector size to be specified in the image labels) to describe most MOC-NA (and WA) images. The model allows low-order polynomial adjustments to the spacecraft position and pointing history in order to register the images to the globally adjusted MOLA coordinates [Smith *et al.*, 2001]. Many MOC images are also affected by high-frequency pointing variations (“jitter”) that cannot be corrected with the available software for image control. Jitter in the stereobase direction gives rise to topographic artifacts in the form of stripes across the DTM; these can be suppressed by high-pass filtering. Severe jitter at right angles to the stereobase interferes with matching; a work-around is to segment the image into regions that can be controlled and DTMs collected separately. MOC stereo DTMs may also contain artifacts in the form of a parabolic height variation across track, caused by uncorrected optical distortions in the camera. The ideal approach to correcting this type of DTM artifact is to account for optical distortion in the sensor model used to make the model. Unfortunately, at the time of the work reported here, the SOCET SET pushbroom sensor model contained a bug that caused optical distortion coefficients to be ignored. We therefore corrected our MOC DTMs, where necessary, by fitting and subtracting a parabolic ridge or

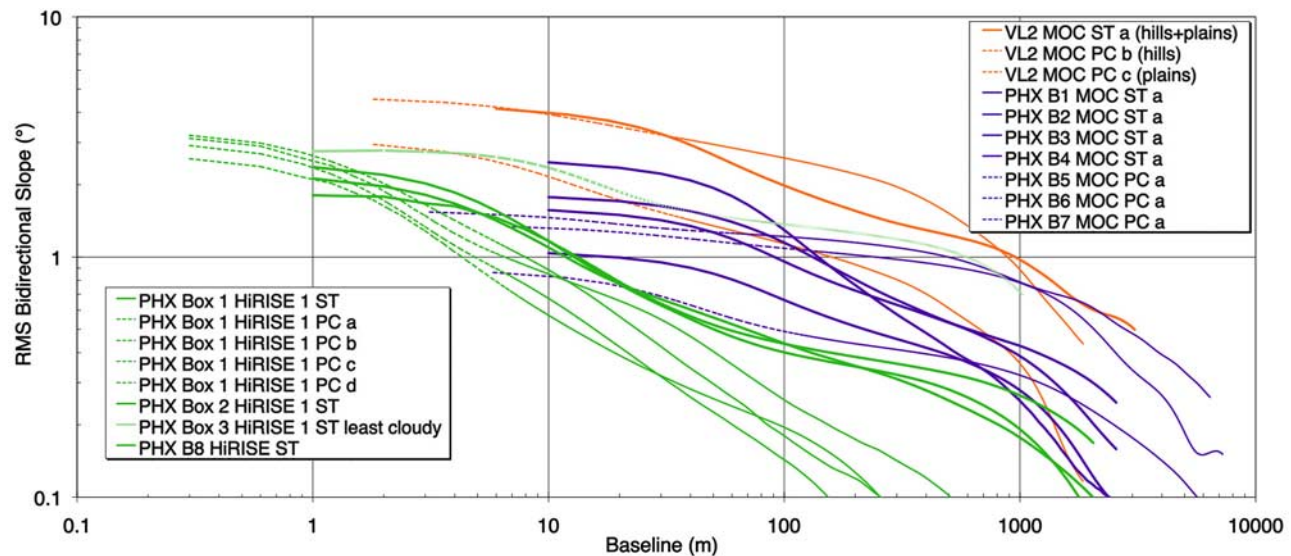


Figure 2. Root-mean-square (RMS) bidirectional slope (slope along a profile) as a function of the baseline over which it is measured, for various candidate landing sites. (orange) terrains near the Viking 2 landing site (a Phoenix site analog) as sampled by MOC images. (purple) MOC results for various sites in Phoenix region B, where the leading candidate was located until High Resolution Imaging Science Experiment (HiRISE) images revealed dangerous rock abundances. MOC results for other locations in the same latitude zone are generally similar; see Table 1. (green) HiRISE results for the three final candidate sites (boxes 1 to 3) and one location in the former candidate region B. Solid curves are used for data from stereo (ST), and dotted curves are for photogrammetry (PC) data. Curve for PHX box 3 is dashed to emphasize that the slopes as shown are probably an upper limit on the true slopes, because poor image quality caused the small-scale texture of the digital topographic models (DTMs) to be dominated by artifacts. See *Kirk et al.* [2003b] to compare additional curves of this type for a variety of candidate sites and the locations where Viking 1, Mars Pathfinder, and the Mars Exploration rovers (MER) landed successfully. The candidate Phoenix sites are smoother than any of these with the exception of the MER B Opportunity site in Meridiani Planum.

trough from the elevations. Although some real topography could also be removed by this process, the effect on estimated slopes should be minimal, because slopes are determined more by local features than by the smooth overall shape of the DTM.

[10] The two-dimensional PC algorithm of Kirk [*Kirk, 1987; Kirk et al., 2003a*] was used to construct DTMs of selected image regions with single-pixel resolution. Accuracy of these DTMs depends crucially on the validity of photometric assumptions, in particular, on the atmospheric haze contribution to a given image, which is essentially an unknown. Misestimating this haze level leads to errors in the overall scale of topography (and slopes). We therefore calibrate the PC analysis by choosing a haze estimate that gives results consistent with a priori topographic data (stereo or MOLA). Tests with simulated and real data suggest that photogrammetry calibrated in this way yields 10–20% relative accuracy for height differences and slopes [*Kirk et al., 2003a*].

2.4. MOC Mapping Results

[11] Our stereo DTMs confirm the impression from MOLA that relief in the candidate landing sites is generally less than 100 m, but the effective resolution of at best 3 pixels (i.e., 10 or 20 m) is inadequate to resolve the decameter-scale patterned ground fully, leaving a concern that it might be dangerously rough over short distances. The

photogrammetric DTMs do resolve decameter features, however, and demonstrate that the patterned ground does not roughen the surface dramatically over baselines between 3 and 10 m. Root-mean-square (RMS) slopes over the shortest baseline measured for each site are summarized in Table 1. The range of values, 0.8–4.5°, is comparable to results for the MER landing sites in Meridiani Planum (1.2–2.5°) and Gusev cratered plains (2.3–4.4°). Figure 2 shows the variation of slope with baseline in region B; results for the other regions span a similar range of roughness at short baselines. The flatness of the curves for baselines <50 m indicates that there are no major slope hazards lurking at or just below the limit of resolution of our data. These results do not, however, constrain the hazards from features substantially smaller than our 3- to 10-m resolution, such as rocks or localized slopes at the edges of the patterned-ground polygons.

[12] Our results also provide information about slope distributions, in particular, the steepest slopes present. At the baselines probed by MOC, slopes exceeding the 16° safety criterion are present over small areas near the rims of relatively fresh craters, but are not found on more subdued pedestal craters. In evaluating overall site safety, the entire mapped area of fresh craters (which constitute only a small fraction of the site) is usually considered “fatal,” even though excessive slopes only occur on a small part of each crater. Even with this conservative assumption, the results

of topographic mapping with MOC were consistent with an acceptable probability of landing safely in any of the regions studied.

2.5. Landing Site Down-Selection Before HiRISE

[13] Rock distributions, the other surface property relevant to landing site safety, were also generally benign as revealed by MOC. Fields of large boulders could be identified in association with craters in some areas [McGrane and Golombek, 2006], but the fraction of the landing sites covered by these fields was only a few percent, and the fraction of the fields covered by boulders was $\sim 1\%$, so that the overall hazard they posed was acceptable [Marlow *et al.*, 2006; Golombek *et al.*, 2008b]. With no significant differences in engineering safety to discriminate between regions, the list of candidates was shortened on the basis of likely accessibility of subsurface ice. Region D was deselected following the first Phoenix Landing Site Workshop in December 2004. Regions A and C were eliminated following the third Workshop in November 2005, and three subareas within the remaining region B were identified for intensive study [Arvidson *et al.*, 2006, 2008]. It was well recognized that the high-resolution images from HiRISE would be crucial to final evaluation of the candidate sites and could potentially transform the perception of the sites' safety. Imaging in support of Phoenix was therefore one of the top priorities for HiRISE between its arrival in its mapping orbit in October 2006 and the end of atmospheric conditions useful for imaging, expected in December. The three region B boxes were to be imaged most intensively, but additional targets in the other regions and throughout the latitude zone would also be imaged as the orbital geometry permitted. A few HiRISE images were also targeted while the MRO spacecraft was in a transitional orbit prior to October. Meanwhile, MOC was to target additional images and stereopairs of the boxes starting as soon as they were illuminated by the Sun in early 2006 and continuing through the entire period of atmospheric clarity.

[14] The first HiRISE images of region B threw these orderly plans for further evaluation and down-selection to a single landing site into disarray by revealing areas of extremely high rock abundance [Smith *et al.*, 2007; Golombek *et al.*, 2008b]. The site selection strategy was quickly altered to a search throughout the latitude zone for areas of low rock abundance as estimated on the basis of predawn temperatures from Mars Odyssey THEMIS thermal IR images and verified by manual and automated rock counts in HiRISE images. Three such areas were eventually found, two in region D and one in region A, and a single HiRISE stereopair of each was obtained along with more widespread monoscopic coverage (Figure 3). One HiRISE pair in region B had also been acquired before the search for new sites began. These four stereopairs became the primary focus of our subsequent investigation into the slope safety of the candidate Phoenix sites.

3. HiRISE

3.1. Image Characteristics

[15] The HiRISE camera [McEwen *et al.*, 2007] is characterized by high SNR and large image size in addition to high resolution. The focal plane contains a total of 14

charge-coupled device (CCD) arrays (Figure 4), each of which operates as a 2048-pixel-wide line detector to build up an image in pushbroom mode, with up to 128 lines of time delay and integration (TDI) to ensure a high SNR even in shadows and near the terminator. The large size of the images minimizes the "edge effects" that hamper automated image matching near the boundaries of the coverage. The combination of high SNR, low compression, and excellent resolution of small features such as rocks leads, in most cases, to an abundance of surface detail that greatly facilitates stereomatching of the images.

[16] Ten of the detectors, filtered to accept only red wavelengths, overlap slightly in the cross-track direction to provide continuous coverage of a swath 20,048 pixels wide. The wide image provided by the red detectors is of greatest utility for stereoanalysis, as well as for many morphologic studies. Additional detectors sensitive to blue-green and near-infrared wavelengths permit false-color imaging of the central 4000 pixels of the swath. The along-track length of images that can be acquired depends on the number of CCDs used, pixel binning (if any), and data compression, but can be as much as 120,000 lines at full resolution. At this size, a single HiRISE pair yields more topographic information than was contained in the entire global DTM of Mars that was produced by the USGS from Viking Orbiter images in the 1980s [USGS, 1991; Batson and Eliason, 1991]. Only the availability of digital or "softcopy" photogrammetric tools running on high-speed workstations make the generation of DTMs from such large images practical.

[17] As discussed in section 2.3, the problem of "jitter" (small motions of the spacecraft around its nominal pointing that distort the scanned image) was identified for Mars Orbiter Camera (MOC) images [Kirk *et al.*, 2003b]. If the amplitude of motion were the same, jitter would be more of a problem for HiRISE because of its higher resolution. In addition, the distortions will occur at slightly different places in the images from different CCDs, complicating the assembly of the full image. This occurs because the detectors are displaced alternately forward and aft in the focal plane as shown in Figure 4, so that they can overlap across track to build up a continuous swath. The same feature therefore crosses the overlapping detectors at slightly different times. In addition, because the reflecting optics of HiRISE obscure the central part of the field of view, the entire detector assembly sits slightly behind the optical axis in the down-track direction. The slight ($\sim 0.5\%$) radial optical distortion of the camera therefore displaces features both along track and across track at the location of the detectors by on the order of 50 pixels. The varying across-track displacement also made it necessary to mount the individual CCDs with rotations ranging from zero to 0.25° relative to the cross-track direction to ensure that ground features stay in the same detector column during the time delay integration. All of these factors (jitter, detector offsets, detector rotations, and optical distortion) must be (and, in our processing, are) taken into account during the reconstruction of the images in order to obtain precision cartographic products. Users wishing to perform their own photogrammetric analyses with HiRISE data should note in particular that many of the images released on the HiRISE website (<http://hirise.lpl.arizona.edu>) are not suit-

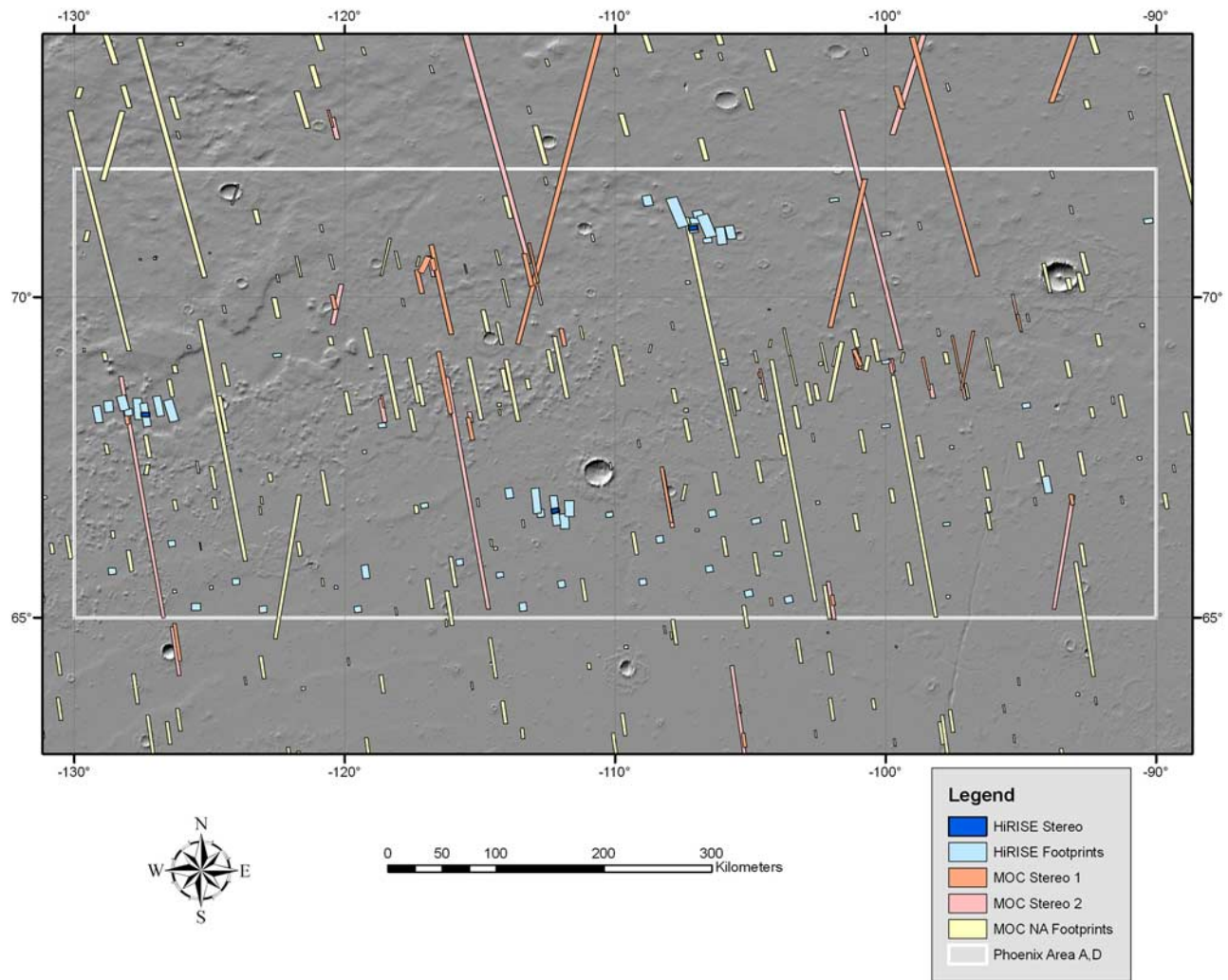


Figure 3. Map of MOC and HiRISE coverage in Phoenix candidate landing site regions A + D (latitude 65–72°N, longitude 230–270°E). Stereopairs are shown in dark colors, unpaired images are shown in lighter colors. The final three candidate sites, boxes 1 to 3 (left to right), are marked by the concentrations of HiRISE images, shown in blue. One HiRISE stereopair was obtained in each site before worsening atmospheric conditions in December 2006 prevented further imaging. The Phoenix spacecraft landed successfully in box 1 on 25 May 2008.

able; these are often quick look products, in which geometrically raw data from the individual CCDs have been mosaicked in their approximate relative positions without corrections for any of the effects listed. Files produced in this way are also included in the NASA Planetary Data System (PDS) archive as extras, and are located in subdirectories of <http://hirise-pds.lpl.arizona.edu/PDS/EXTRAS/RDR/>. They may be identified by the incorporation of “NOMAP” (for “not map projected”) in the filenames. The assembled images known as Reduced Data Records (RDRs) in the PDS archive at <http://hirise-pds.lpl.arizona.edu/PDS/RDR/> are also unsuitable for photogrammetric analysis. These products have been corrected for optical distortion, detector coordinates, and spacecraft motion as modeled by the standard mission trajectory and pointing data (SPICE kernels [Acton, 1999]), but they have also been orthorectified to map coordinates by projection onto a surface defined by MOLA altimetric data. This process

removes the parallax corresponding to any details that are resolved in the topographic model used. Orthorectification with the standard MOLA MEGDR gridded product leads to objectionable piecewise-linear deformation of the images at the 463-m grid spacing of the altimetry. HiRISE processing therefore makes use of a version of the MEGDR that has been smoothed with three passes of a 7×7 pixel low-pass boxcar filter. The data set is temporally padded at its eastern and western ends with data from adjacent longitudes before the filtering steps, in order to avoid introducing discontinuities at the boundaries. Stereo processing of the RDRs will reveal a “high-pass-filtered” version of the Martian surface that includes only those details that are not seen in the smoothed MOLA model. Thus, to achieve accurate mapping results from HiRISE stereopairs, one should start with the geometrically “raw” Experimental Data Records (EDRs) available at <http://hirise-pds.lpl.arizona.edu/PDS/EDR/> and orientation data in the form of NAIF SPICE

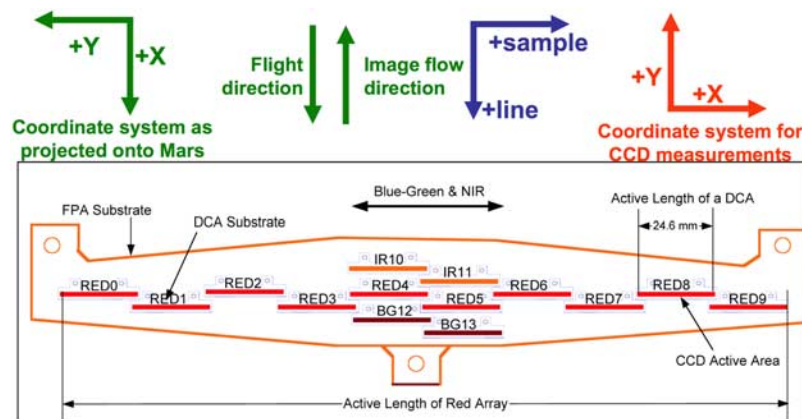


Figure 4. HiRISE focal plane assembly showing charge-coupled device (CCD) detector arrays. CCDs 0–9 are used to acquire the full-width red-filter image. Detectors 10–11 and 12–13 obtain near-infrared and blue-green band images, respectively, of the central 20% of the swath. Green arrows show how the detectors would be oriented with respect to the Mars Reconnaissance Orbiter (MRO) frame (X forward, Y left, and Z to Mars) if the HiRISE optics were “unfolded” and viewed from behind. This is thus the relative positioning of the instantaneous images from the separate CCDs on the Martian surface. A different coordinate system (red) was used for collecting measurements of CCD positions with respect to the focal plane assembly. The HiRISE optical axis intersects the detector approximately 94 mm below the center of the detector pattern in the orientation shown here.

kernels and use either the ISIS software described in section 3.3 or some equivalent set of processing steps to assemble the EDRs into a full-width image in which geometric distortions have been corrected.

[18] The stereo parallax generated by the along-track offset of the different detectors is negligible for topographic mapping purposes ($\sim 0.03^\circ$). Stereo coverage is therefore obtained by rolling the spacecraft (rotating it around the flight direction to point to the side of the nadir ground track) to obtain a second image of a previously acquired target on a later orbit that passes nearby. For features at low latitude, such rolls provide a cross-track stereobase that is within a few degrees of being east-west and that aligns with the sample direction of the images. At high latitudes, the situation is more complex; to image the pole, for example, the spacecraft must be rolled to the poleward side of its inclined orbit on both opportunities. In this situation, both images are oblique, the stereobase is primarily along track, and stereo parallax is mainly in the line direction. Targeting of stereopairs requires a complex tradeoff between optimal convergence angle (typically $20\text{--}25^\circ$ but smaller angles are preferred for very rough terrain and vice versa), minimizing the delay between images to avoid surface changes and large shifts in illumination conditions, avoiding low-phase angles (which yield low-contrast images that are difficult to stereomatch), and avoiding conflicts with other observations. An early goal of the HiRISE team has been to gain experience about what imaging geometries and camera settings lead to acceptable stereopairs for both interactive viewing and DTM production.

3.2. Geometric Calibration

[19] The complex design and extremely high resolution of the HiRISE camera lead to the requirement for a large amount of geometric calibration information, if the stereo DTMs produced are to be free of systematic errors and thus to have an accuracy that approaches their high precision.

The same factors of complexity and resolution unfortunately made collecting the required calibration information extremely challenging. Even if the calibration equipment in the laboratory approached the resolution of HiRISE and if adequate time had been available to collect a dense set of calibration observations (neither of which was the case), substantial changes to the structural dimensions and optical properties of the camera were expected in flight, as a result of the lack of gravitational distortions, vibrations at launch, and the slow drying of the support structure. We therefore adopted a multistage approach to developing a full geometric model of the HiRISE optics, in which data from a variety of sources were combined and cross-checked wherever possible. The relative positions of detectors were measured directly in the laboratory. Ray-trace results based on the HiRISE optical design were used to obtain an initial estimate of the focal length and a model of the shape (and complexity) of higher-order optical distortions. A limited number of calibration observations, in which points on each CCD were surveyed through the optics to establish the relation between focal plane position and exterior angles, provided a rough confirmation of the camera model based on the first two steps. Imaging of star fields at several times during the cruise from Earth to Mars provided a more sensitive check of the model and allowed a final improvement of the focal length value. The star observations also placed an upper limit on errors in the measured focal planes, though more precise bounds may come from the accumulated images of Mars.

[20] The numerous coordinate systems for describing the focal plane assembly (FPA) offer considerable potential for confusion. Because of the folded optics of the camera, the FPA actually lies in the Y - Z plane of the MRO spacecraft, perpendicular to the flight direction. Figure 4 shows the FPA as viewed from the illuminated side, with a coordinate system that has $+X$ to the right and $+Y$ upward. This is the

Table 2. HiRISE Focal Plane Assembly Coordinates^a

CCD	X_0 (mm)	Y_0 (mm)	dX/dS (mm)	dX/dL (mm)	dY/dS (mm)	dY/dL (mm)
0	-96.3935	112.9956	-0.000057	0.012000	-0.012000	-0.000057
1	-89.4914	88.9950	-0.000042	0.012000	-0.012000	-0.000042
2	-96.9459	65.0469	-0.000034	0.012000	-0.012000	-0.000034
3	-89.4927	41.0380	-0.000018	0.012000	-0.012000	-0.000018
4	-96.4998	16.9992	0.000002	0.012000	-0.012000	0.000002
5	-89.4960	-7.0010	-0.000001	0.012000	-0.012000	-0.000001
6	-96.6811	-30.9996	0.000019	0.012000	-0.012000	0.000019
7	-89.4935	-55.0034	0.000031	0.012000	-0.012000	0.000031
8	-96.3954	-78.9990	0.000049	0.012000	-0.012000	0.000049
9	-89.1039	-102.9997	0.000056	0.012000	-0.012000	0.000056
10	-110.9610	16.9991	0.000000	0.012000	-0.012000	0.000000
11	-103.6857	-7.0010	-0.000001	0.012000	-0.012000	-0.000001
12	-82.2033	16.9993	0.000002	0.012000	-0.012000	0.000002
13	-74.9334	-7.0007	0.000003	0.012000	-0.012000	0.000003

^aPixels to millimeters. See equations (1a) and (1b) for definitions. HiRISE, High Resolution Imaging Science Experiment; FPA, focal plane assembly; CCD, charge-coupled device.

local coordinate system in which CCD positions were measured. For photogrammetric purposes, however, it is useful to consider how the FPA would be oriented if the HiRISE optics were “unfolded” and the detectors were viewed in the orientation that corresponds to their projection through the optics and onto the surface of Mars. In this orientation, the MRO + X axis (the direction of flight) is downward with respect to Figure 4, + Y is to the left, and + Z (the direction to Mars) is into the page. Coefficients relating pixel coordinate to focal plane position in millimeters were derived in this coordinate system. A further complication was that the arbitrary origin for the FPA measurements corresponded neither to the center of the detector field (the so-called “HiRISE boresight”) nor to the optic axis of the camera, from which the “boresight” is offset by approximately 94 mm. Direct measurements were made of the X and Y coordinates of a fiducial mark at the left side of each CCD, and of the Y coordinate only of a mark at the right side, with a nominal precision of 0.1 μ m. These measurements were used, along with the pixel spacing (12 μ m in both the line and sample directions, which are assumed perpendicular), detector dimensions of 128 lines and 2048 samples, and the designed offset between the detector pixels and the fiducial marks, to determine a set of coefficients giving affine transformations from pixel coordinates (S , L) to (X , Y) in millimeters and the reverse:

$$X = X_0 + \left(\frac{dX}{dS}\right)S + \left(\frac{dX}{dL}\right)L, \quad (1a)$$

$$Y = Y_0 + \left(\frac{dY}{dS}\right)S + \left(\frac{dY}{dL}\right)L, \quad (1b)$$

and

$$S = S_0 + \left(\frac{dS}{dX}\right)X + \left(\frac{dS}{dY}\right)Y, \quad (2a)$$

$$L = L_0 + \left(\frac{dL}{dX}\right)X + \left(\frac{dL}{dY}\right)Y. \quad (2b)$$

[21] Numerical values for the coefficients in equations (1) and (2) are given in Tables 2 and 3, respectively. X and Y are given in the “unfolded” coordinate system as discussed above, with the origin located where the optical axis intersects the focal plane. The sample and line values are referenced to an origin at the center of each two-dimensional CCD array. Because the dimensions (128 \times 2048) of the detectors are even, this midpoint is located between adjacent pixels in both the line and sample directions, and the line and sample coordinates of pixel centers relative to this origin therefore have half-integer values. Sample number S , as defined for the HiRISE EDR products that are provided to the Planetary Data System, increases to the right in Figure 4. (These files are produced by combining two lower-level files that contain data from the two sides of the detector. In order to read out each image line from the detector before the next line is taken, the data from the two sides of the detector are read out in opposite directions through separate electronic channels, doubling the speed of the readout process. While in principle the data from the two channels can be “stitched” back together without any distortion, the reading out of the data in opposite directions presents another opportunity for confusion. The raw data onboard the camera, and played back to Earth, has the two channels presented as mirror images. One channel must therefore be “flipped” before it can be matched to its companion. The EDR products have the flipping already completed to avoid problems for the users.) Note that the line coordinate L is not related to the line at which a feature may occur in a HiRISE image file, which corresponds to the time at which the feature was imaged. Instead, L indicates the pixel position within the detector array at the midpoint of the interval of time delay and integration. If all 128 TDI lines are being used, this is the center of the detector, $L = 0$. Otherwise, the effective position of the observation is biased toward the readout side of the CCD, which is at the top in Figure 4, according to the formula $L = (128 - \text{TDI})/2$ where TDI is the number of TDI lines employed. Thus “no” time delay integration corresponds to TDI = 1 and yields an effective detector position $L = -63.5$. L increases downward as shown in Figure 4. Similarly, the detector sample coordinate S , which is in the range -1023.5 to 1023.5 ,

Table 3. HiRISE Focal Plane Assembly Coordinates^a

CCD	S_0	L_0	dS/dX (mm ⁻¹)	dS/dY (mm ⁻¹)	dL/dX (mm ⁻¹)	dL/dY (mm ⁻¹)
0	9378.1524	8077.2934	-0.394667	-83.332399	83.332399	-0.394667
1	7389.8315	7483.7943	-0.294667	-83.332812	83.332812	-0.294667
2	5397.7384	8094.0967	-0.235333	-83.333001	83.333001	-0.235333
3	3408.5206	7462.8992	-0.126333	-83.333238	83.333238	-0.126333
4	1417.7277	8041.4541	0.011667	-83.333333	83.333333	0.011667
5	-584.1893	7457.9416	-0.008667	-83.333333	83.333333	-0.008667
6	-2570.4742	8060.8598	0.132667	-83.333228	83.333228	0.132667
7	-4564.4476	7469.5375	0.214000	-83.333059	83.333059	0.214000
8	-6550.2948	8059.8497	0.341333	-83.332634	83.332634	0.341333
9	-8548.7314	7465.1052	0.387000	-83.332435	83.332435	0.387000
10	1416.5929	9246.7458	0.000000	-83.333333	83.333333	0.000000
11	-584.4516	8640.4070	-0.010000	-83.333333	83.333333	-0.010000
12	1417.9481	6850.0007	0.016333	-83.333332	83.333332	0.016333
13	-581.9435	6244.5851	0.019333	-83.333331	83.333331	0.019333

^aMillimeters to pixels. See equations (2a) and (2b) for definitions.

should not be confused with the integer coordinate of a sample in an image from this single CCD or in the assembled image covering the entire field of view.

[22] In order to determine the focal length and optical distortions of the HiRISE camera as designed, the optics software package ASAP from Breault Research was used to trace rays from an array on a nominal ground plane at $Z = 300$ km from the camera, through the optics and onto the focal plane [Gallagher *et al.*, 2005]. A total of 1515 points, spaced every 60 m across track and 64 m along track were used. Given the focal length of the camera, approximately 12 m, the corresponding focal plane coordinates spanned the area occupied by the CCD detectors (Figure 5a). The correspondences between the ground coordinates (X, Y) and the focal plane coordinates (x', y') were used to obtain least squares estimates of the parameters in the camera model defined as follows. First, the ground coordinates are related to “ideal” focal plane coordinates (x, y) for a camera with focal length f by the colinearity equations

$$x/f = X/Z, \quad (3a)$$

$$y/f = Y/Z. \quad (3b)$$

where the origin is taken to be the principal point, i.e., the intersection of the optical axis with the focal plane. The observed focal plane coordinates (x', y') are then assumed to be related to the ideal coordinates (x, y) by a purely radial transformation

$$x'/r' = x/r, \quad (4a)$$

$$y'/r' = y/r, \quad (4b)$$

where

$$r' = \sqrt{x'^2 + y'^2}, \quad (5a)$$

$$r = \sqrt{x^2 + y^2}. \quad (5b)$$

Finally, the distortion $\Delta r = r' - r$ was modeled by a polynomial of the form

$$\Delta r = k_0 r' + k_1 r'^3 + k_2 r'^5 + \dots, \quad (6)$$

which differs slightly from standard usage in that Δr is frequently expressed as a polynomial in r rather than r' [Wolf, 1983, pp. 102–104]. For small distortions, the two types of polynomial will be similar, though not strictly identical.

[23] The parameters in these equations are redundant in one respect: both f and k_0 affect the scale of the image in the focal plane. To remove this redundancy, we chose k_0 to satisfy the requirement that the positive and negative extremes of Δr within the detector area be equal and opposite; this choice minimizes the errors that result if the distortion correction is not applied. The corresponding value of f is known as the calibrated focal length [Wolf, 1983, pp. 74–80]. Our expectation in fitting the ray-trace points was that, although the focal length of the real instrument might differ significantly from the designed value, the radial distortion should be similar. At a minimum, the order of the polynomial required to fit the ray-trace distortions should apply to the real camera, but in all likelihood the values of the coefficients should be similar as well. Figure 5a shows the ideal and observed positions of the ray-trace points in the focal plane; the apparent curvature of the straight rows of points caused by the $\sim 0.5\%$ pincushion distortion is readily visible. Figure 5b shows the radial distortion pattern $\Delta r(r')$. A fit with highest-order term r'^3 yielded a RMS radial residual of $0.73 \mu\text{m}$. More importantly, these residuals had a systematic dependence on r' indicating that the inclusion of higher-order terms would improve the fit. Including a r'^5 term in the distortion polynomial decreased the RMS radial residual to $0.55 \mu\text{m}$, equivalent to 0.05 detector pixel, with no systematic dependence on r' . The calibrated focal length and coefficients of the distortion polynomial are given in Table 4. We also checked the residuals of the ray-trace data to the camera model for evidence of tangential distortion. The RMS tangential distortion was $0.13 \mu\text{m}$, or roughly 0.01 pixel, which was considered to be negligible.

[24] Laboratory observations of one fiducial mark per CCD array through the HiRISE optics provided an indication of how much the actual focal length differed from the

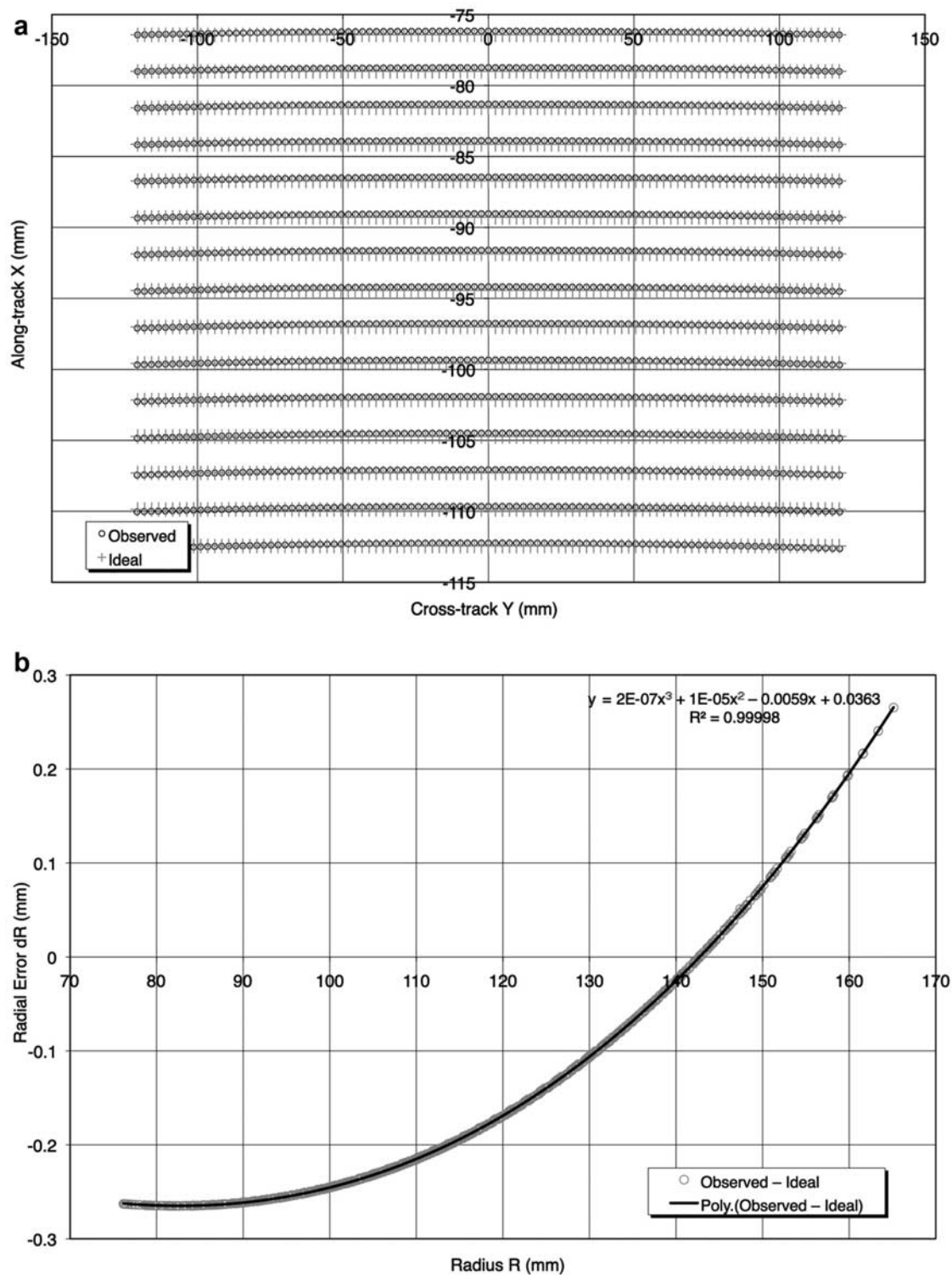


Figure 5. Optical distortion model fitted to ray-trace calculation on the basis of HiRISE camera design. An array of 1515 regularly spaced ground points were projected into the camera, covering the area of detector arrays shown in Figure 4. (a) Focal plane coordinates of points as observed (with distortions) and for an ideal camera with the same focal length but no distortions. Curvature in the focal plane of the straight lines of points on the ground is readily apparent without exaggeration. Coordinate system is that for the “unfolded” camera with respect to the MRO frame, so Figure 5 is rotated 180° relative to the orientation of Figure 4, and the optical axis is above the detector area shown. (b) Plot of radial distortion as a function of radial distance from optical axis, with polynomial fit (equation (6)). RMS residuals to fit are 0.00055 mm (0.05 pixel).

Table 4. HiRISE Focal Lengths and Optical Distortion Coefficients^a

Parameter (units)	Value	Comments
f (mm)	12055.53	At ∞ , raytrace
	11960.19 \pm 50	At ∞ , laboratory
	11988.19 \pm 50	At ∞ , lab corrected for focus
	11995.00	At ∞ , Stellar M calibration
	11995.48	At Mars (recommended)
k_0	-0.004850857	
k_1 (mm ⁻²)	2.41312×10^{-7}	
k_2 (mm ⁻⁴)	-1.62369×10^{-13}	

^aSee equations (3)–(6) for definitions.

designed value, but the estimated measurement errors of 0.58 mm (~ 50 pixels) combined with the small number of points made it impossible to assess optical distortion with this data set. The effective focal length derived from these observations was converted to a calibrated focal length based on the theoretical distortion model. The resulting value, given in Table 4, has an uncertainty of 0.4% and differs from the design value by 0.8%.

[25] Observations made during the cruise phase of the MRO mission provided the primary means of assessing the focal length and distortion of the real camera. Stellar images, including focus tests, were obtained on three separate dates in order to quantify the relaxation of the instrument toward its equilibrium dimensions and optical properties as the epoxy structure dried. The Omega Centauri cluster was imaged in September 2005, the “Wild Duck” cluster (Messier 11) was imaged in October, and the “Jewel Box” (NGC 4755) was imaged in December as part of an observation sequence referred to as “Stellar M.” The first two sets of observations revealed a fundamental difficulty resulting from the optimization of the HiRISE camera and MRO attitude control system (ACS) for observations of Mars: rapid scanning of the sky leads to short exposure times and relatively few identifiable stars, but slowing the scan rate to provide longer exposures leads to relatively large oscillations about the desired orientation, probably as a result of propellant sloshing. The internal distortions of the star images caused by these oscillations severely impacted our automated procedures for identifying the imaged stars.

[26] Our procedure was to start with the proto-EDRs (the EDR format was not finalized in the early part of the cruise). These files were ingested into ISIS 3 (using the hi2isis program), then crudely calibrated (using hiclean), stitched

together to form a CCD-level file (histitch), cosmetically cleaned (with cubenorm), and output in the FITS format (isis2fits). Flexible Image Transport System (FITS) is the standard for many astronomical data sets [Wells et al., 1981; Hanisch et al., 1999]. The commercial program PinPoint from DC-3 Dreams (<http://pinpoint.dc3.com/>) was used to (1) identify stars in each FITS file, (2) produce a list of visible stars in the area from a variety of astrometric star catalogs, (3) match the stars in the image to those in the catalog, and (4) output data in a delimited text format conducive to further analysis. This process was largely automated using the scripting capability of PinPoint. However, when the images were significantly internally distorted, the software was not able to match the observed stars with those in the catalog. Furthermore, our first stellar target, Omega Centauri, is so dense a star cluster that most star catalogs, including the Tycho 2 catalog [Hog et al., 2000] used for HiRISE calibration do not list any stars near its center. It was therefore not possible to match the observed stars to precise astrometric coordinates in this area.

[27] The first two sequences were nevertheless successful as focus tests, and we made a limited number of manual star measurements that were used to determine the relative alignment between the star tracking cameras of the ACS and HiRISE. To simplify mission operations, the overall coordinate frame for the MRO spacecraft is defined in terms of HiRISE, with its Z axis in the direction of the HiRISE “boresight,” more properly, the look direction of the left-most (in the orientation of Figure 4) sample of CCD 5. Coordinate frames for the star cameras and the HiRISE optical axis are defined in terms of this MRO frame.

[28] By the time of the Stellar M observation, we were able to use ISIS program skymap to transform the images to celestial coordinates (i.e., map project them onto the sphere of the sky), thereby removing enough of the internal distortion to increase the success of automated star measurement significantly. The choice of a scan rate intermediate between those of the Omega Centauri and M11 observations was also helpful. In all, about 1500 star measurements were obtained from three image sets repeating sequence CRU_000016 and five from CRU_000027, for a total of ~ 100 stars in each of the 14 CCDs.

[29] The star coordinates measured by PinPoint in the reprojected images, as well as the catalog coordinates of each star, were transformed back into the raw camera geometry by using the ISIS 3 program skyptr. The camera-space residuals between the observed and catalog positions

Figure 6. HiRISE star calibration results from “Stellar M” observations of December 2005. (a) Residuals for three repetitions of sequence CRU_000016 (identified by symbol color) plotted against relative time from 0 at start of image to 1 at its end. A small number of outlier points have been removed. Note repeatability of fluctuations caused by spacecraft jitter. Smooth curves through the residuals, computed by sliding mean and sliding polynomial fit give nearly identical models of the jitter; the polynomial model was used to dejitter the residuals for further analysis. The nonzero mean values of the residuals along and across track are not significant, because the final definition of the MRO coordinate frame in relation to the HiRISE boresight had not been determined at the time these data were taken. (b) Dejittered cross-track residuals plotted as a function of cross-track coordinate in samples. Three repetitions of sequence CRU_000016 and five of CRU_000027 are shown in red and blue, with separate polynomial fits. Parabolic curvature of trendlines plausibly results from the detector arrays being mislocated by about 5 mm from the center of optical distortion (model shown by green line). Overall slope of residuals indicates a need to correct the focal length value used. (c) Dejittered along-track residuals plotted against cross-track coordinate. Linear trend indicates a slight yaw rotation of the spacecraft with respect to scan direction. Offsetting the detectors to fix the across-track residuals increases this rotation error slightly (green curve).

of individual stars show surprisingly large variations within the image, up to 50 pixels. Plots of the residuals against relative time within the image sequence (Figure 6a) reveal a pattern of “jitter” oscillations that repeats with remarkable fidelity each time the sequence is executed. We therefore

fitted a smooth curve to the residuals as a function of normalized time for each sequence and used this curve as a model of the jitter in order to correct the individual residuals. After correcting the observations in this way, we were able to identify and reject 4 measurements out of

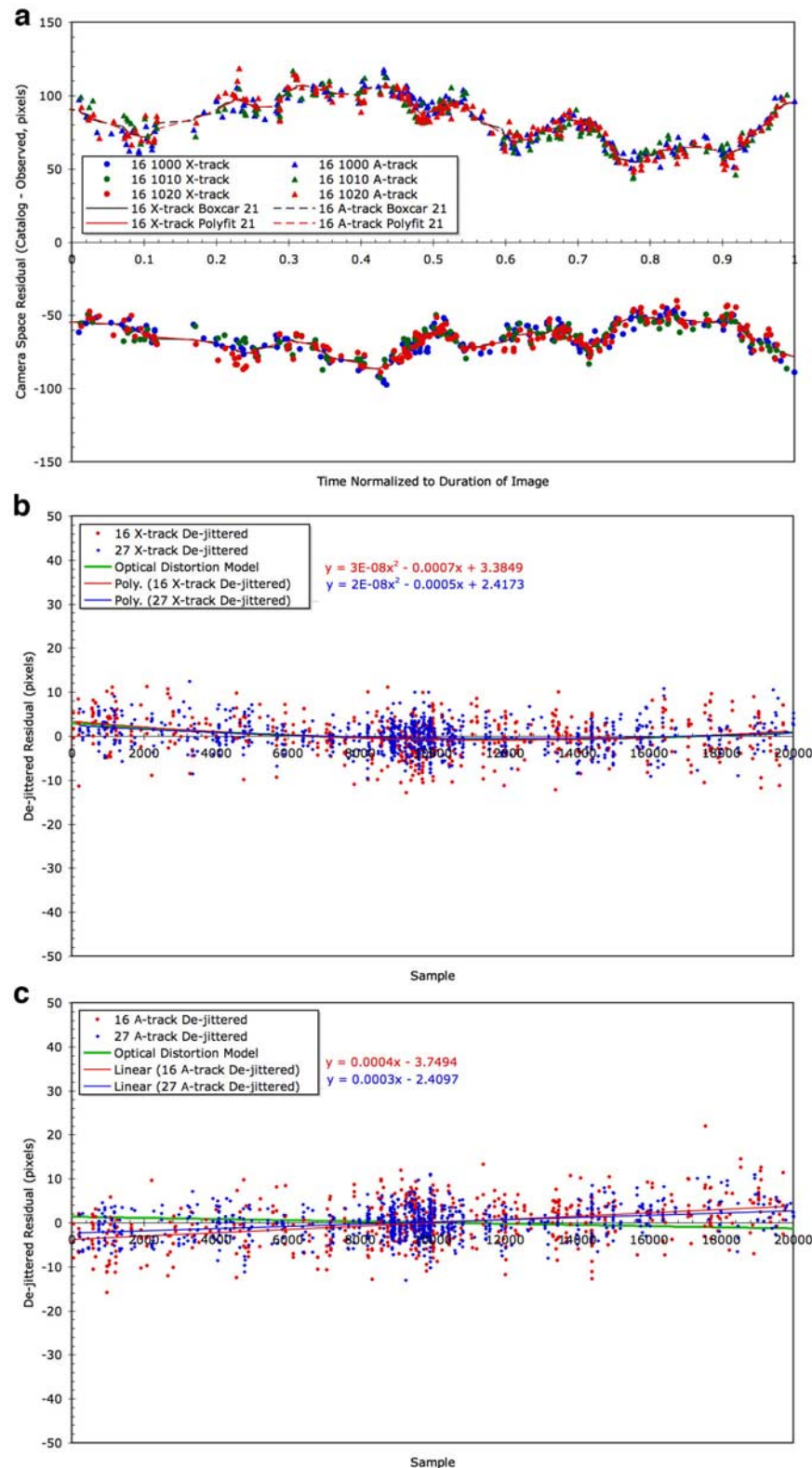


Figure 6

Table 5. HiRISE Mounting Angles^a

Rotation	Name	Around Axis	Value (°)
ω	Roll	X	0.06553
ϕ	Pitch	Y	0.44153
κ	Yaw	Z	0.0

^aSequential rotations ω , ϕ , κ relate the HiRISE camera frame defined by the instrument optical axis to the Mars Reconnaissance Orbiter (MRO) spacecraft frame.

567 from sequence CRU_000016 and 60 out of 921 from CRU_000027 as stars misidentified by the automated software, with residuals many times higher than the remainder of the population. Figures 6b and 6c show the jitter-corrected residuals as a function of cross-track position within the focal plane. Several systematic patterns are evident and are consistent between the two image sequences. The quadratic variation of cross-track residuals can be explained if the detector arrays are located about 5 mm to one side of their nominal position with respect to the optical axis, so that the radial distortion pattern is centered at a different location in the image. The slight linear trend of cross-track residuals is indicative of an error in the focal length used to project the sky data into the camera. The linear trend in the along-track residuals results partly from the miscentering of the radial distortion pattern and partly from a small misalignment of the camera about the look direction (yaw rotation). Each of these effects is of the order of 5 pixels or less across the 20,000-pixel field of view. We have corrected the cross-track scale discrepancy (linear trend) by adopting the revised focal length estimate shown in Table 4. The other effects could be corrected by adjusting the positions of the detectors with respect to the optic axis and making a compensatory change of the rotation matrix between the HiRISE optical axis and the MRO frame defined by the HiRISE “boresight.” The DTMs described in this paper were produced before such adjustments were made. The resulting distortions of these models should be a small fraction of a meter, because the two images of each stereopair are nearly aligned so that the distortions largely cancel between the two images. We have subsequently adjusted the detector positions and the HiRISE mounting angles and confirmed that these refinements to the camera model eliminated the residual cross-track distortion while retaining the correct alignment of the instrument relative to the attitude control system. The detector coordinate information in Tables 2 and 3 and the mounting angles in Table 5 reflect these adjustments.

[30] Figures 6b and 6c show no evidence for other systematic effects, such as a change in the along-track position of the FPA with respect to the optical distortion pattern or a modification in the radial distortion pattern itself. Figures 6b and 6c also indicate that the relative positions of the CCDs given in Tables 2 and 3 do not need to be updated in light of the star observations; if they did, offsets between the points corresponding to stars in different detectors would be apparent. Given the RMS scatter of the residuals (about 4 pixels) and the ~ 100 measurements available per CCD, an upper limit of $\sim 4/\sqrt{100} = 0.4$ pixels or $5 \mu\text{m}$ can be placed on the errors in the relative positions of the CCDs. The mean residuals for each CCD do not differ significantly from zero at this level of precision.

[31] The focal length estimated from laboratory observations can be adjusted for the effects of refocusing the camera in flight and compared with the corrected focal length based on the star observations. Each millimeter that the second fold mirror is translated in order to adjust the focus changes the focal length by 32.85 mm. Allowing for the measured shift in the best focus position between the laboratory calibration and the Stellar M observations yields the focal length estimate shown in Table 4, which has an uncertainty of 0.4% and lies within 0.06% of the focal length based on the star calibration residuals. The latter result has an estimated accuracy of 0.01% or better (i.e., ≤ 1 pixel out of 10,000 from the center to edge of the field of view) and is therefore preferred. For use in modeling images of Mars, the “focal length” (actually, the rear principal point distance, but this parameter that determines the image scale is often referred to informally as focal length) must be corrected for refocusing of the camera from infinity to a range $Z = 300$ km according to the formula $1/f(Z) + 1/Z = 1/f(\infty)$. The resulting correction is 0.48 mm, or $\sim 0.004\%$.

3.3. Software Development

[32] Topographic mapping with HiRISE images makes use of both the USGS ISIS system and the commercial stereogrammetric software SOCET SET in much the same way as for MOC [Kirk *et al.*, 2003b], Mars Express HRSC [Kirk *et al.*, 2006a], and numerous other planetary image data sets. Within this broad outline, two aspects of HiRISE processing deserve comment as distinct from our past efforts. In the past, images were ingested, and initial processing was performed in the ISIS 2 software system. HiRISE is the first instrument to make use of the object-oriented successor system ISIS 3 [Anderson *et al.*, 2004; see also <http://isis.astrogeology.usgs.gov>] and therefore also the first instrument for which it was necessary to create software to translate image data and supporting metadata between ISIS 3 and SOCET SET formats. The ISIS 3 processing pipeline for HiRISE images is described by Becker *et al.* [2007]. A full radiometric calibration capability was not yet available, so for this study we made use of images radiometrically calibrated to first order at the level of individual detectors and “balanced” between detectors at the University of Arizona. Translation of data from ISIS 3 to SOCET SET follows the same set of steps as for ISIS 2: the image data are written to an unlabeled or “raw” binary file by using the ISIS program *isis2raw*, and a new program (*isishi2socet*) making use of standard ISIS utility routines reads the support data from the ISIS labels and writes out a “settings file” that contains the equivalent information about camera parameters, spacecraft trajectory, and pointing in a text format recognized by SOCET SET. Finally, running the existing SOCET SET image importation procedure causes the raw image to be converted to Vitec tiled format for internal use and a “support file” (detached label) containing the camera and spacecraft data to be created and associated with the image. For the work described in this paper, we used previously written translation software (*dem2isis2* and *ortho2isis2*, respectively) to export DTMs and orthorectified images from SOCET SET in the form of ISIS 2 cube files for further processing. The ISIS 2 format can be used directly by ISIS 3 software, but we have since

implemented the capability for exporting data from SOCET SET directly to ISIS 3.

[33] A more significant challenge was posed by the geometric complexity of the HiRISE camera. SOCET SET provides a “generic” sensor model (i.e., software that computes the transformation between image coordinates and ground coordinates) for pushbroom scanners, which we have successfully used for MOC and HRSC processing. Unfortunately, this software cannot be used to model raw HiRISE images at the level of accuracy required because it does not allow the detectors to be located away from the axis of radial optical distortion. Rather than develop our own sensor model specific to HiRISE, we have elected to preprocess the images in ISIS to remove the optical distortion so that the existing sensor model can be used. The ISIS 3 program *noproj*, written for this purpose, transforms input images by projecting them into ground coordinates of latitude and longitude and then back into the image coordinates of an idealized, distortionless HiRISE camera that can be modeled in SOCET SET. Other geometric effects are corrected at the same time: data from the offset and rotated real CCDs are transformed to what a single, straight detector would have seen, so that they can be mosaicked together and treated as a single image. To the extent that the “jitter” motions of the platform are known, these can be corrected by *noproj* as well, so that the ideal image is what would have been seen from a more stable platform. We will return to the issue of jitter in section 4.1. Finally, we note that the generic pushbroom sensor model contained several bugs that made mapping with HiRISE and other line scanner images impossible. We negotiated with BAE Systems to obtain access to the sensor model source code and were able to fix these bugs. Our bug fixes will be included in new releases of SOCET beginning in early 2009, but in the meantime, we can provide the corrected sensor model to researchers using SOCET SET for Mars mapping in compiled form, for use as a “plug in” to the software.

3.4. Initial Testing and Procedure Development

[34] The tools that must be developed for stereomapping with a new type of image data include not only software, as discussed in the previous section, but a complete set of procedures for working with the images from ingestion through DTM production. In the case of HiRISE, the main procedural issues to be addressed involved the ISIS 3 preprocessing steps needed to assemble the data from multiple CCDs into a single image for mapping purposes (this can be considered a problem of determining the relative control needed to bring the subimages together seamlessly), absolute geodetic control of the assembled images to the coordinate system defined by MOLA, and “tuning” of the automated stereomatching algorithm in SOCET SET to produce DTMs with maximum resolution and minimum need for editing to remove spurious features. The HiRISE data sets used for the initial development and testing of such procedures were those covering the locations of the MER Opportunity and Spirit. These data sets are also useful for illustrating the improvement in DTM resolution (horizontally and vertically) from MOC to HiRISE, because both areas had previously been mapped and both contain features of various scales that can be compared.

[35] The 750-m diameter crater in Meridiani Planum, informally named Victoria, was the first feature to be mapped with HiRISE because of the urgent need to navigate Opportunity safely around, into, and eventually back out of the crater. Three HiRISE images of Victoria had been obtained and were processed: TRA_000873_1780 (0.267 m pixel⁻¹, 3.75° emission), PSP_001414_1780 (0.276 m pixel⁻¹, 17.54°), and PSP_001612_1780 (0.265 m pixel⁻¹, 1.95°). In all cases, the spacecraft was east of the crater, so the convergence angle is approximately the difference of the respective emission angles. The expected vertical precision EP, assuming 0.2-pixel matching error [Kirk et al., 2003b], is 0.22 m for a stereopair consisting of the first two images and 0.19 m for the second and third images. The latter pair was used for DTM production. In addition, we had previously generated a DTM (unpublished) at 5 m post⁻¹ from ~1.6 m pixel⁻¹ MOC images R14-00021 and S05-00863, with EP of 0.44 m.

[36] For this project we treated the images from individual CCDs (after *noproj*) as independent. Only the two or three red detector segments that overlapped the crater were used; segments from each of the three HiRISE images were adjusted together. The ultimate source of control was the MOLA MEGDR, but to avoid the difficulty of identifying common features between HiRISE and MOLA, which differ in resolution by several orders of magnitude, we used coordinates measured from the 1.5 m pixel⁻¹ MOC images previously controlled to MOLA for horizontal control. This also ensured that the two data sets would be registered to one another even more precisely than they are tied to MOLA. A total of 33 features within ~1 km of the crater were measured interactively: 5 with horizontal coordinates weighted at 10 m, 22 with heights weighted at 3–5 m, 1 with both, and 5 as tiepoints with no ground coordinates assigned. Most points were measured on four overlapping images, resulting in an average of 16 points per image. Because of the narrow (~1°) field of view of HiRISE, it is neither possible nor necessary to adjust both camera position and pointing. We adjusted the spacecraft position (with a weighting of 1000 m along track, 100 m across track, and 10 m radially) and the rotation around the camera axis (weighted at 0.02°), but held the remaining pointing angles fixed. Linear drifts of these parameters were also permitted. Spacecraft positions for all images moved consistently about 1000–1700 m along and 260 m across track. The magnitude of these offsets was surprising, and we initially attributed this to our use of predicted rather than reconstructed ephemerides for these images. As described subsequently, however, shifts of comparable size have been required for subsequent stereopairs for which the standard MRO mission ephemerides were available and used. The resolution of this puzzle is described later in this section. With a looser radial weighting, the spacecraft also moved vertically by 500 m. With the 10-m weighting, RMS residuals were 9.4 m in longitude, 26.5 m in latitude, 7.9 m in elevation, and 0.86 pixels in the images (line and sample errors combined). We believe that the large residuals are attributable to an error that we made in producing the unpublished MOC DTM that was used as a control base. This data set agrees in east-west scale but appears to be about 11% too large north-south compared to the HiRISE images (held close to the nominal spacecraft

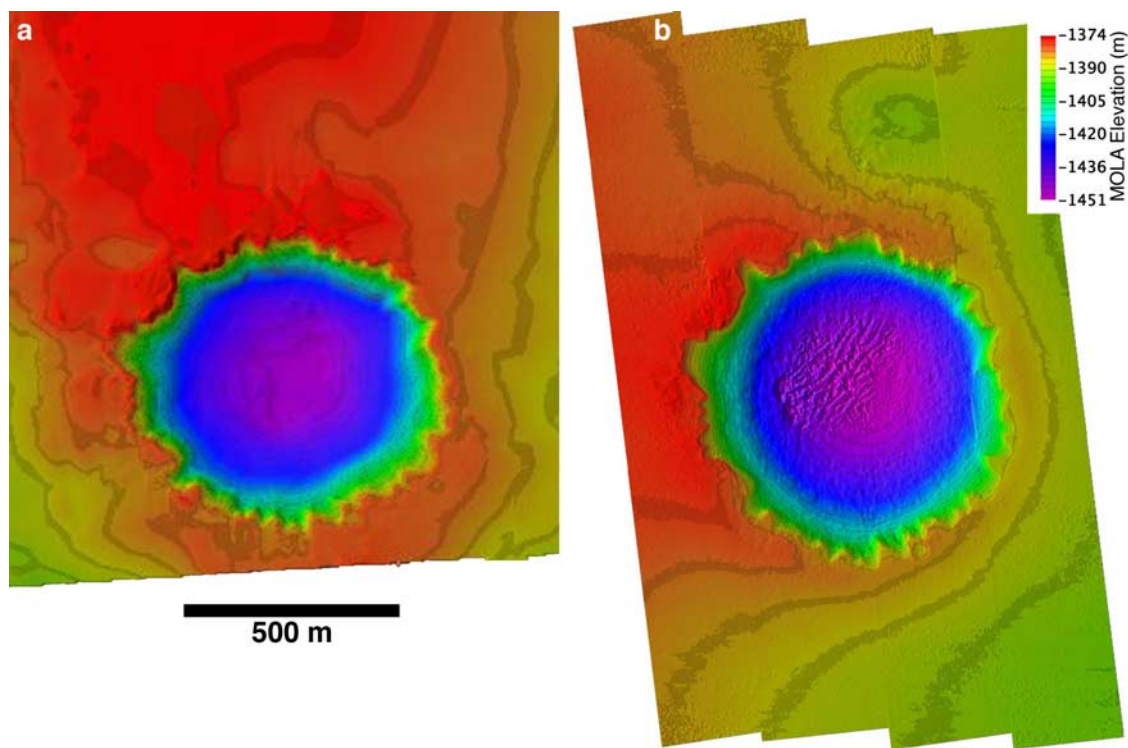


Figure 7. Color shaded relief maps of the informally named crater Victoria, currently being explored by the MER Opportunity Rover. Contour interval is 3 m. (a) Stereo DTM data collected manually from MOC images. Grid spacing is 10 m post^{-1} , but only a relatively small number of identifiable features (particularly around the rim of the crater) were measured, and the remainder of the data set was interpolated. The high elevation of the midline of the model compared to the left and right edges is an artifact caused by uncorrected radial distortion in the MOC optics. (b) Stereo DTM collected by automatic matching of HiRISE image data, with limited manual editing done to select and smooth areas where severe artifacts resulted because the surface was entirely featureless, very steep, or both. The edges of the shadow of the crater rim, which fell at different locations in the two images, were erroneously matched and were also edited, but image details inside the shadows were matched successfully. Small undulations (unrelated to real image features) in the flattest part of the plains surrounding the crater correspond to RMS matching errors on the order of 0.2 image pixel. Discontinuities along the diagonal seams between HiRISE detectors result from uncorrected “jitter” motions of the spacecraft and have an amplitude $\leq 1 \text{ m}$.

altitude), the MOC images as projected in ISIS, and the rover track as reconstructed photogrammetrically from images taken on the ground [Li *et al.*, 2007a, 2007b], which can be compared to the rover locations and tracks visible in the HiRISE images. The large horizontal errors with respect to the resolution of the images are disappointing, but it is clear that the two data sets are controlled consistently at a precision better than the $\geq 100\text{-m}$ accuracy with which either can be located relative to MOLA, if not at the pixel scale.

[37] This first study area proved to be extraordinarily challenging for automated stereomatching. The Meridiani plains are extremely flat and covered primarily by fine material that appears featureless at HiRISE resolution [Squyres *et al.*, 2006]. Sedimentary outcrops and eolian ripples less than a meter high provide image texture in a few areas, but much of the region surrounding the crater is featureless apart from a scattering of small rocks and faint streaking with windblown dust. The interior slopes of the crater are similarly bland but relatively steep (up to 30°).

Outcrops in the crater walls are vertical and many are deeply shadowed. We previously found it almost impossible to match images of the Meridiani plains at MOC resolution [Kirk *et al.*, 2003b] and resorted to interactive measurements to obtain the MOC DTM of Victoria. Despite these challenges, we obtained a useful DTM over most of the crater and surroundings by automatic matching of the HiRISE images PSP_001414_1780 and PSP_001612_1780 (Figure 7). Results in bland areas were improved considerably by applying a difference-of-Gaussians (DOG) band-pass filter [Vosselman *et al.*, 2004] to the images, followed by a contrast enhancement, for the final passes of the multi-resolution, multipass matching strategy. The standard strategy for “adaptive” ATE [Zhang and Miller, 1997] performs eight matching passes, beginning with images reduced in resolution by averaging of blocks of 32×32 pixels and ending with 2×2 averaged images. This strategy was applied to produce a DTM with 2-m grid spacing based on the full resolution, unfiltered images. The result from ATE was then refined by performing two more matching passes

with nonadaptive ATE and the filtered images, first with 2-m grid spacing and then with 1-m spacing. The DOG filter was implemented by low-pass filtering the images in ISIS with a Gaussian kernel with width parameter (standard deviation) of 1 pixel and then high-pass filtering the result with a Gaussian having a standard deviation of 2 pixels. The high SNR of HiRISE permitted accurate matching within deep shadows, but the change in position of the shadow edges between images resulted in unavoidable artifacts. The shadow edge areas were interactively edited to follow the ground surface as visible in a stereoscopic view of the images. Areas on the surrounding plains and particularly on the sloping but bland floor of the crater that had severe matching artifacts (with a characteristic angular pattern that we refer to informally as “snow angels” or “Maltese crosses”; for an example, see Figure 13g) were interactively selected and smoothed. The duneforms on the crater floor were also poorly matched and would require extensive editing to produce an accurate DTM: the automatic algorithm easily matched the sharp dune crests, but did not follow the ground in the smooth, bland areas between the crests. These features pose a known hazard to the rover, which is therefore unlikely to approach them closely. We therefore decided not to expend the effort that would be needed to edit the DTM in this area.

[38] Small variations in the apparent height of the plains, with a random spatial pattern (i.e., not associated with landforms seen in the images and not having the characteristic “Maltese cross” shape of the much more severe artifacts found in the blandest areas of the images), have an RMS amplitude of 0.2 m. In comparison, the “ground truth” from the rover indicates that most areas around Victoria crater are covered by eolian ripples with amplitudes of only a few centimeters [Sullivan *et al.*, 2007]. Larger ripples with wavelengths between 1 and 2 m are seen in the HiRISE images in some areas. These resemble the large ripples encountered between the landing point and Victoria, and probably have similar amplitude of 30–40 cm, but they are not resolved by the DTM. Thus, the 0.2-m RMS amplitude of variations in plains areas of the DTM can plausibly be attributed to random errors in matching and can be used to quantify those errors. The excellent agreement of Figure 7 with the expected vertical precision EP calculated above indicates that the RMS matching error is, indeed, close to 0.2 pixels. Comparison of our DTM with those generated by Li *et al.* [2007b] from MER Pancam stereo-pairs shows that estimated depths and slopes of inlets such as Duck Bay and Bottomless Bay are closely consistent. Surface missions such as MER presently provide the only data sets that exceed or even approach the resolution of HiRISE, so such comparisons are especially valuable. Overall, the expectation of a substantial improvement in DTM detail from the fivefold improvement in pixel scale and several-fold improvement in SNR relative to MOC is clearly fulfilled.

[39] The density and contrast of surface detail visible in the second stereopair used for testing, covering the Spirit landing point in Gusev crater and the entire rover traverse to and through the informally named Columbia Hills, is strikingly superior to that in the Victoria images and, in fact, much more representative of the HiRISE images on the whole. Our second DTM was produced from images

PSP_001513_1655 (0.261 m pixel⁻¹, 4.10° emission) and PSP_001777_1650 (0.268 m, 15.79°), which have a convergence angle of 19.8° and a predicted EP of 0.16 m.

[40] For this project, subimages from all 10 red CCDs were rectified with noproj, mosaicked, and controlled and processed as a unit. The initial results obtained in this way were disappointing: the SOCET matching algorithm performed well when data from the same CCD detector in both images was compared, poorly wherever data from one CCD overlapped a different detector in the other image. This problem was quickly understood to result from along-track offsets of the odd and even CCDs in each image by about 5 pixels, which introduced enough parallax in the direction perpendicular to the stereo base to prevent the matcher from finding corresponding points. Multipixel offsets in the stereo base direction were also present, leading to vertical jumps (“cliffs”) with amplitudes of several meters in the DTM at the CCD-CCD boundaries. These mismatches cannot be the result of errors in our knowledge of the CCD positions in the focal plane, or equally large mismatches would have been seen in the star calibration data (Figure 6). Instead, they must be caused by errors in knowledge of the spacecraft pointing and rotation rates. The across-track offset corresponds to a yaw knowledge error of roughly 0.5°, and the along-track offset to a pitch rate error of ~1% or 0.0005° per second. The phenomenon is fundamentally the same as “jitter” discussed in sections 2.3 and 3.1, but, whereas we expected to see pointing errors come and go over hundreds or thousands of lines, the dominant errors are almost (but not completely) constant over the tens of thousands of lines of the images, which are acquired at a rate of ~10,000 lines per second. A satisfactory solution to the problem was achieved by shifting the CCD images to the best nearest-pixel alignment (as determined by manual feature measurements) before mosaicking.

[41] Although a MOC DTM and previously controlled images were available in this area, the HiRISE images were controlled directly to the MOLA data. We did, however, refer to the THEMIS DTM previously produced by Kirk *et al.* [2005] to be sure that the images fell on the Columbia Hills; the MOLA DTM was less useful for this purpose because few MOLA ground tracks sampled these features (for comparison, see Figures 8a and 8b). Because the initial mismatch to MOLA was again several kilometers, it was useful to measure a few (six) horizontal control points and perform an initial adjustment. In general, we find it extremely helpful when searching for features to provide horizontal control to bring the ungridded MOLA elevation points (from the Precision Elevation Data Records, or PEDRs, available at <http://pds-geosciences.wustl.edu/missions/mgs/pedr.html>) into SOCET SET. By displaying these points along with the imagery and elevation contours from the MEGDR, one can be sure to choose control features that were actually sampled by MOLA rather than features in areas where the MEGDR contains interpolated data. With the alignment to MOLA improved, an additional eight points were selected for vertical control and assigned elevations from the MEGDR. Suspecting (incorrectly, as discussed below) that the large offsets might result from errors in the HiRISE mounting angles being used, we initially adjusted only the camera angles. The final adjustment included both angles

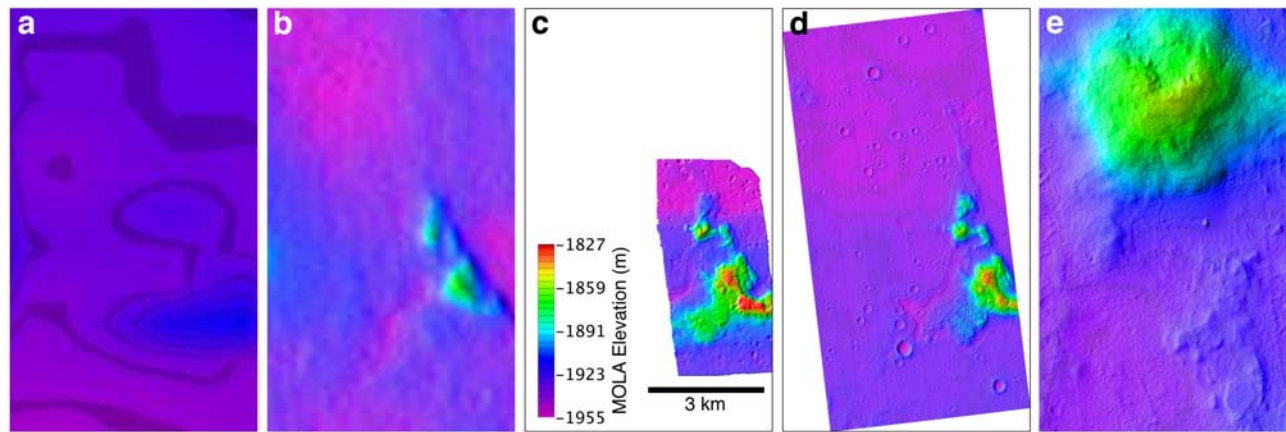


Figure 8. Topographic models of the MER Spirit landing point and vicinity, including the informally named Columbia Hills, on the floor of Gusev crater. The same color coding of elevation is used in all images. All but the last, which is enlarged 10 \times , show the same 6.4 \times 11 km area. (a) Mars Orbiter Laser Altimeter (MOLA) global data set (MEGDR) at 462 m post⁻¹ omits the hills entirely because of gaps between altimetry profiles. (b) Shape-from-shading applied to a composite of Thermal Emission Imaging Spectrometer (THEMIS) IR and visible data at 80 m post⁻¹. (c) MOC stereo DTM at 10 m post⁻¹, covering the hills but not the landing point. Note horizontal “banding” of the DTM, caused by spacecraft jitter adding spurious parallax. (d) Full extent of HiRISE stereo DTM, showing \sim 6-km wide swath. Minor discontinuities between data from the individual HiRISE detectors are visible in the plains, but are \leq 1 m high. (e) Enlargement of HiRISE DTM to show full detail at 1 m post⁻¹. Husband Hill is the major peak at top. Current rover location is near Home Plate, the circular plateau at lower right (both names are informal). Note the small bump immediately below Husband Hill; this is the most severe matching artifact in the DTM. One of the detector seams is also faintly visible near the right edge of the image.

(weighted at 0.5°) and position (at 100 m horizontally, 10 m vertically), though the angular weight corresponds to more than 2000-m shift at ground level, so a similar result could be obtained without adjusting the positions. Linear drifts of the angles and positions were also permitted but were weighted tightly (0.0001° per second and 1 m s⁻¹), so that ground coordinates at the beginning of the end of the images could adjust only a few meters relative to one another. The final RMS residuals were 6.03 m in longitude, 17.9 m in latitude, and 0.04 m vertically.

[42] The large adjustments of position or pointing that were needed to register the HiRISE images to MOLA came as an unpleasant surprise. Although the adjustment process described here should ensure that output products are consistent with MOLA, we would naturally prefer to understand and eliminate the causes of the large offsets and eliminate them. As described in the next section, the Phoenix sites were mostly so smooth that determining the horizontal positioning of the images relative to MOLA was impossible. The DTMs of more rugged sites that we subsequently produced for the HiRISE team provided additional clues, however. These models continued to require adjustments much larger than the estimated uncertainty of the MRO trajectory and pointing data. The best ephemerides for the mission, computed on the basis of a post-MRO gravity model, have an estimated accuracy of a fraction of a meter (A. Konopliv, written communication, 2007). The standard reconstructed ephemerides that we use were found to be consistent with the high-precision products to within about 5 m for orbits at the beginning of the mission, and to within 1 m for later orbits (B. Semonov, written communication, 2008). Both types of ephemerides

are available as SPICE SPK kernels from <ftp://naif.jpl.nasa.gov/pub/naif/MRO/kernels/spk/>; the high-precision products can be identified by the presence of “mro95a” in the filenames. The reconstructed pointing is available in a single version as SPICE CK kernels from <ftp://naif.jpl.nasa.gov/pub/naif/MRO/kernels/ck/>. The precision of the CKs is less well known, but the MRO pointing knowledge requirement is 0.035 mRad, which corresponds to \sim 10 m on the ground. Remaining systematic errors in pointing may be somewhat larger, but probably no greater than 0.3 mRad or 100 m on the ground. One constraint on such errors comes from the two observation sequences of the Stellar M calibration, which had nonzero mean residuals even after adjustment of the star-tracker to HiRISE alignment. Residual errors in both the roll and pitch directions ranged from \sim 0.15 to 0.3 mRad, suggesting a constant pointing bias on the order of 0.2 mRad and variable errors on the order of 0.1 mRad. Thus, the large adjustments we found necessary for images of Mars cannot be explained in terms of errors in the a priori data we used.

[43] The largest component of error in the a priori positioning of the images in SOCET SET, an along-track shift of as much as 1.7 km at midlatitudes, was traced to confusion over coordinate systems. Because SOCET SET uses planetographic latitude, we had referenced camera angles to a planetographic system, i.e., to the local vertical relative to the ellipsoidal reference surface of Mars. A close examination of the SOCET pushbroom sensor model revealed, however, that it expects camera angles to be referenced to a planetocentric system with “vertical” along the local radius vector to the spacecraft. Computing the camera orientation with respect to this system eliminated the

Table 6. HiRISE Stereopairs Mapped for Candidate Phoenix Landing Sites

Site	E Lon (°)	Lat (°)	Image 1	Image 2	Res 1 (m)	Emiss ang 1 (°)	Res 2 (m)	Emiss ang 2 (°)	RMS Slope (°)	Baseline (m)	Description
PHX Box1_1	232.6	66.1	PSP_001959_2485	PSP_002091_2485	0.31	0.70	0.32	15.52	2.37	1.0	ST “Green Valley,” region D
									3.12	0.3	PC subarea a
									2.52	1.0	PC subarea a
									2.57	0.3	PC subarea b
									2.11	1.0	PC subarea b
									3.21	0.3	PC subarea c
									2.65	1.0	PC subarea c
									2.91	0.3	PC subarea d
									2.36	1.0	PC subarea d
PHX Box2_1	247.8	66.7	PSP_001919_2470	PSP_001932_2470	0.32	10.80	0.32	12.13	2.12	1.0	ST southern site, region D
PHX Box3_1	252.9	71.1	PSP_001945_2515	PSP_002077_2515	0.31	2.44	0.32	11.68	2.76	1.0	ST northern site, region A (smoothed)
PHX B8	130.3	67.5	TRA_000894_2475	TRA_000881_2475	0.31	0.27	0.34	23.14	1.81	1.0	ST region B

along-track error and left a mostly across-track discrepancy on the order of 200 m between coordinates computed in ISIS and those calculated in SOCET SET. We are currently searching for the source of this remaining shift, which we suspect is also the result of an error or inconsistency in how SOCET SET and our supporting code handle the orientation data. If this systematic error can be eliminated, we will be able to use appropriately tight weighting of the a priori trajectory and pointing data in future adjustments and will obtain more accurate ground coordinates in areas where horizontal control is difficult to identify.

[44] With the relative positions of the CCD images adjusted to the nearest pixel, automatic stereomatching proceeded extremely smoothly. The matching strategy used was a variation on that used for the Victoria DTM: after completion of the eight-pass standard adaptive strategy, the matching pass at 2 m post⁻¹ made use of DOG-filtered images, but the unfiltered images were used for the final pass at 1 m post⁻¹. The resulting DTM is shown in Figure 8 alongside various pre-MRO models of the same area. The poor representation of the hills in the MOLA data set interpolated from rather widely spaced profiles is noteworthy, as is the horizontal “banding” of the MOC stereo DTM, which is the result of spacecraft jitter distorting the model. Nevertheless, when slopes along east-west baselines (i.e., within and thus not distorted by the jitter “bands” in the MOC DTM) are computed, the RMS slopes from MOC and HiRISE data agree to within $\pm 5\%$ for baselines between 10 and 1000 m, providing additional confirmation that the HiRISE stereo results are correct and useful for landing site hazard evaluation. The full detail of the earlier data sets is visible in Figures 8a–8c, but that of the HiRISE DTM is only visible upon further enlargement (Figure 8e). Subtle geologic details are visible in the full resolution DTM, such as the low plateau in the southeast corner Figure 8e, informally known as Home Plate, that Spirit is currently investigating. Comparison of our DTM with recent unpublished results based on applying the methods of Li *et al.* [2007b] to MER Pancam images (R. Li, written communication to MER Athena team, 2007) again indicates that the two data sets yield extremely similar slopes and elevation differences over distances of meters to tens of meters. The

somewhat rough-appearing texture of most of the surface is probably a combination of real features at the limit of resolution and the uncertainty in matching features. The RMS amplitude in the flattest parts of the scene is on the order of 0.2 m, corresponding to 0.3-pixel matching error. Also visible in Figure 8e is one of the CCD-CCD boundaries, along which the elevations are discontinuous by about 0.8 m or less as a result of the uncorrected subpixel mismatches between detectors. Finally, Figure 8e also shows the largest of the isolated artifacts caused by severe matching errors, most of which are only a few posts across. Searching the DTM to find these flaws and interactively editing them out required only 12 h, or 0.22 h per million posts, a substantially lesser effort than the 1 h per million posts we had estimated before the mission. For comparison, the planetary images with the next best matching success, scanned from the Apollo metric and panoramic camera photographs of the Moon, typically require 4 h per million posts. Other, less favorable types of images may require more than 50 h. The Columbia Hills data are typical of the majority of the HiRISE images in terms of surface contrast and signal-to-noise ratio, so very efficient DTM editing should be the rule. The main exception we have identified so far is that HiRISE images of extremely rugged terrain, which contain large numbers of small shadowed areas, may require as much as 2.5 h of editing per million posts.

3.5. Stereo Mapping of Candidate Phoenix Landing Sites

[45] HiRISE acquired one stereopair in the original region B candidate site while in its transition orbit and one pair in each of the new candidate boxes after insertion into the mapping orbit. These images are summarized in Table 6, where we refer to the pair in box 1 as “PHX Box1_1,” and so on, in the expectation that additional stereo coverage of each box will be obtained at the next opportunity. The contrast of most of the images is only slightly degraded by atmospheric haze, but the oblique image for box 3, PSP_002077_2515, contains patchy clouds through which the surface is almost invisible. The images were processed as described in section 3.4 for Columbia Hills, but the ISIS program hijitreg was modified and used to determine the

Phoenix Box_1_1

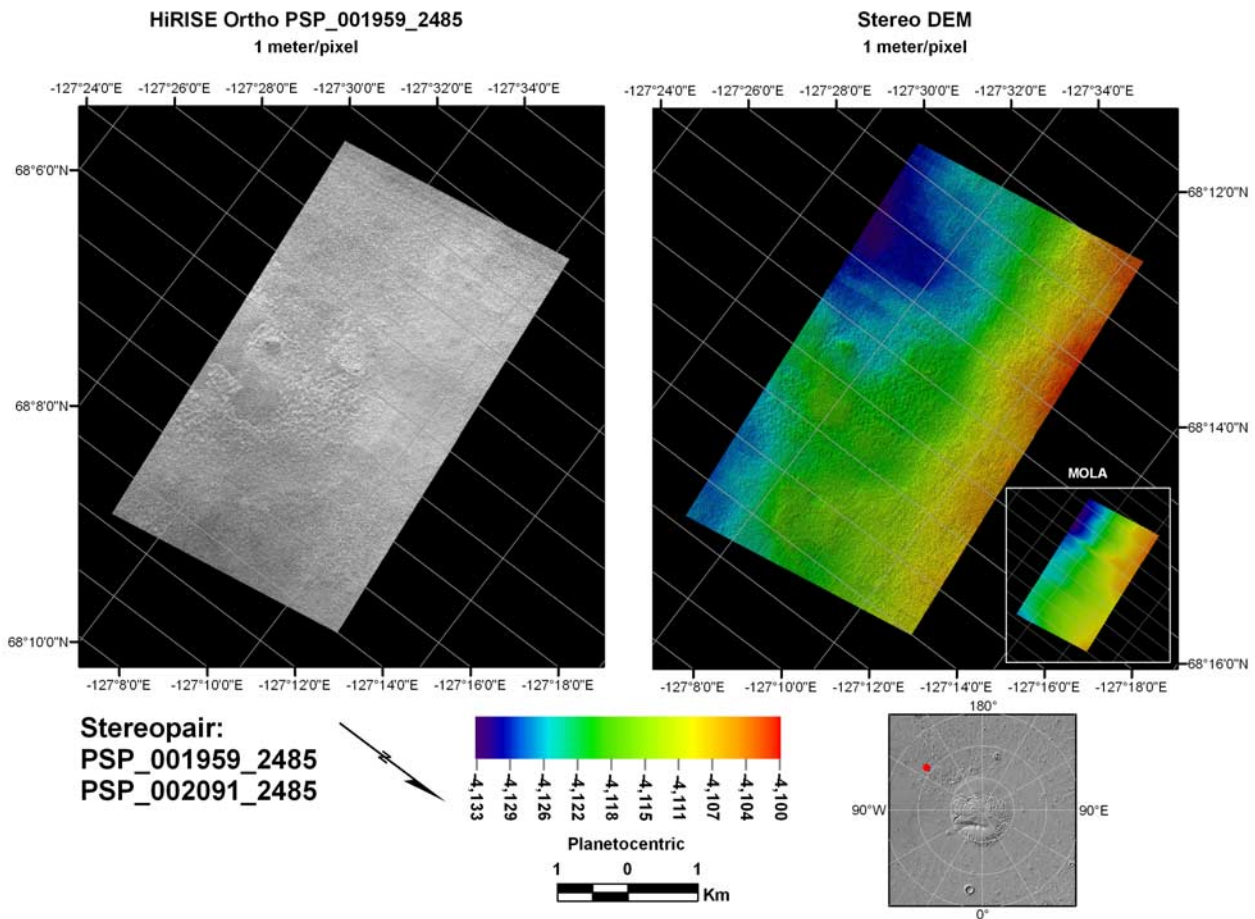


Figure 9. Orthoimage (left) and color-coded shaded relief map (right) of the HiRISE stereopair PSP_001959_2485/PSP_002091_2485 in box 1, the favored site among the final three candidates. Inset shows MOLA altimetry for the corresponding area, and map at bottom shows location in relation to the north pole. The Phoenix spacecraft landed in box 1, approximately 35 km east of the center of this DTM.

nearest-pixel offsets to be applied to the CCD images before mosaicking. The surface morphology in all of the images (Figures 9–12) consists of patterned ground, with abundant texture at scales of meters to decameters but no larger features that are both visible in the images and expressed topographically in the MOLA data set. The total relief as shown by MOLA is only 30 to at most 110 m. As a result, the horizontal location of the stereo DTMs cannot be controlled to MOLA in the usual fashion, though controlling them vertically is straightforward. Between 20 and 50 control points constrained in Z only, plus, in some cases, a handful of unconstrained tiepoints, were selected for each pair. Unfortunately, without horizontal control points, the fit residuals cannot be reported. Parameters for the “nadir” (lower emission angle) image of each pair were held, keeping the pair at approximately its a priori horizontal location, and the parameters for the oblique image were adjusted. The same weights were used as for Columbia Hills, except for the box 3 model, which was weighted more loosely (1° in angle and 300 m across track). The box 3 and B8 DTMs contained distinctive topographic patterns that

could be recognized in the MOLA data and used to measure interactively the horizontal displacement between the respective data sets. In these cases, the support files (labels) for both images of the pair were edited to correct this interactively determined offset. A new DTM that registers more closely to MOLA was then collected. This process of deriving control by comparing a preliminary DTM rather than the images to the MOLA control base is the manual equivalent of the rigorous, automated adjustment process developed by *Spiegel et al.* [2005] for Mars Express HRSC images. By making use of the entire DTM rather than a few selected features, the automated version can control the images with a horizontal accuracy of a fraction of the MOLA grid spacing, provided that the scene contains sufficiently distinctive relief features.

[46] DTMs for the four Phoenix areas were collected by using the standard adaptive strategy, followed by a single additional matching pass using the full resolution images to produce a 1 m post^{-1} DTM. The box 1, box 2, and B8 models and parts of box 3 required only light editing (Figure 13a–13e). Extensive regions of the box 3 model,

Phoenix Box_2_1

Stereopair:
PSP_001919_2470
PSP_001932_2470

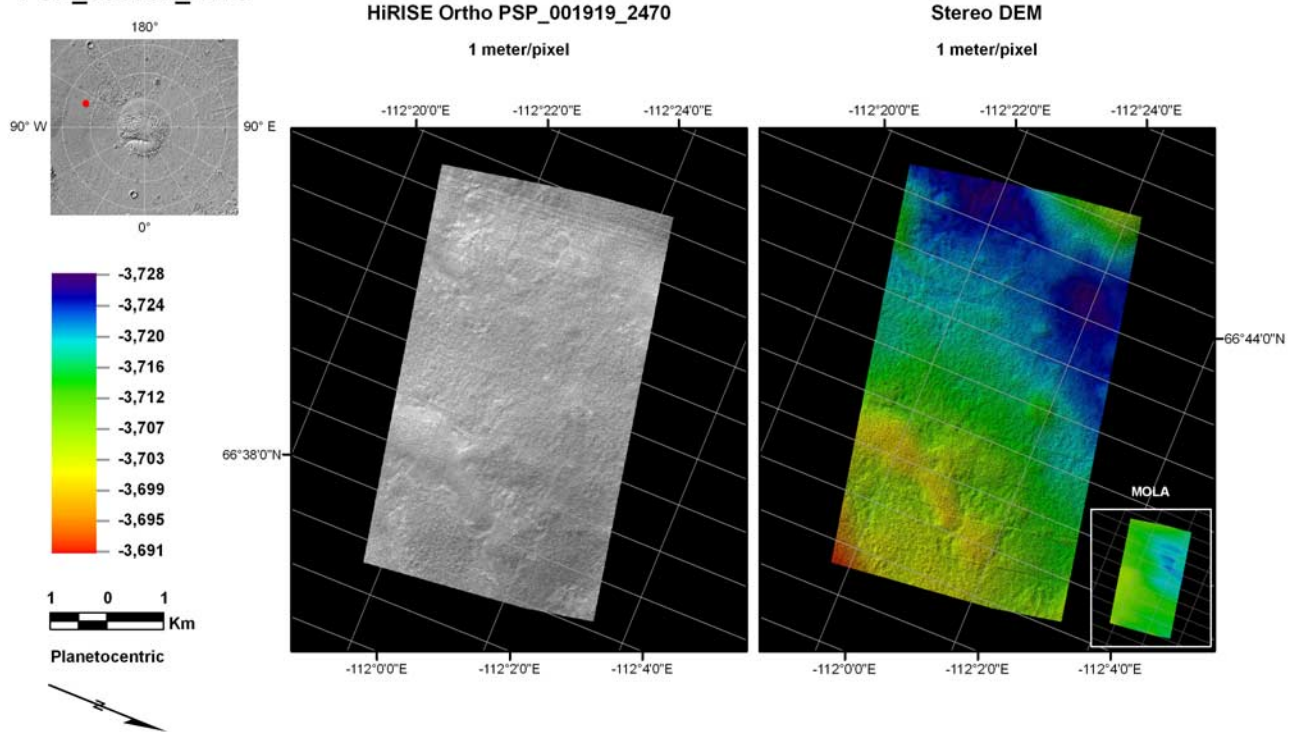


Figure 10. HiRISE stereopair PSP_001919_2470/PSP_001932_2470 in box 2, the second priority among the final candidate sites. Presentation as in Figure 9.

in which the oblique image was particularly cloudy (Figure 13f–13j), were covered by severe matching artifacts in the form of “Maltese crosses” that are the characteristic result of applying the SOCET SET matcher to low-contrast scenes [Kirk *et al.*, 2003b]. Substituting high-pass-filtered and contrast-enhanced versions of the images for the final matching pass improved the DTM quality in moderately cloudy areas but introduced additional noise in the least cloudy areas. We therefore merged the best results from the unfiltered and filtered images. A few areas of very dense cloud cover yielded poor results even after filtering the images. These areas could not be edited to reflect the true surface topography, because the clouds prevented us from seeing the surface visually. The affected areas were therefore smoothed to partially suppress the artifacts, and a mask showing the affected areas was prepared so that statistical analyses of this site could be restricted to the areas of good data.

[47] Figure 2 and Table 6 summarize the slope-statistical results for the four Phoenix sites. Results for box 3 are for a 1024×2400 pixel subarea in the least cloudy part of the images. Even in this area, the local details of the DTM, including slopes, were dominated by recognizable matching artifacts, so the data were smoothed with a 7×7 pixel low-pass filter before statistics were collected. For the other data sets, the entire DTM was rotated to align the boundaries of the data with the line and sample axes, and statistics were

collected over the largest rectangular area that could be inscribed in the data set. The resampling needed to rotate the data set causes slopes over a one-post baseline to be decreased by about 8% relative to the value calculated from unresampled data. This level of smoothing is not significant for landing site certification and was deemed an acceptable compromise in order to sample a large a portion of the site as possible. RMS bidirectional slopes over 1 m (1 post) range from 1.8° for B8 to 2.8° for box 3. The slope-baseline curves in Figure 2 tell a slightly more complicated story: the curves for boxes 1 and 2 and B8 are quite similar overall and are comparable to the smoothest MOC models in region B for baselines from 30 to 300 m that are definitely well resolved by both data sets. Slopes in box 3 are a factor of 4 higher at these long baselines, clearly as a result of the large domical hill that dominates the DTM region (Figure 11), but this is still comparable to the typical MOC results. The slope at 1-m baseline in box 3 must be treated as considerably more uncertain than the other results, because the DTM has been smoothed to suppress what are clearly matching artifacts rather than real features. Any real slopes at the limit of DTM resolution will also be somewhat suppressed as well, but inspection of the DTM (Figure 13) suggests that artifacts still dominate, so that this slope may be an upper limit. The 99th percentile adirectional slopes at 1-m baseline are 8.1° , 7.1° , and 6.6° . These values are about 3.5 times the corresponding RMS bidirec-

Phoenix Box_3_1

Stereopair:

PSP_001945_2515

PSP_002077_2515

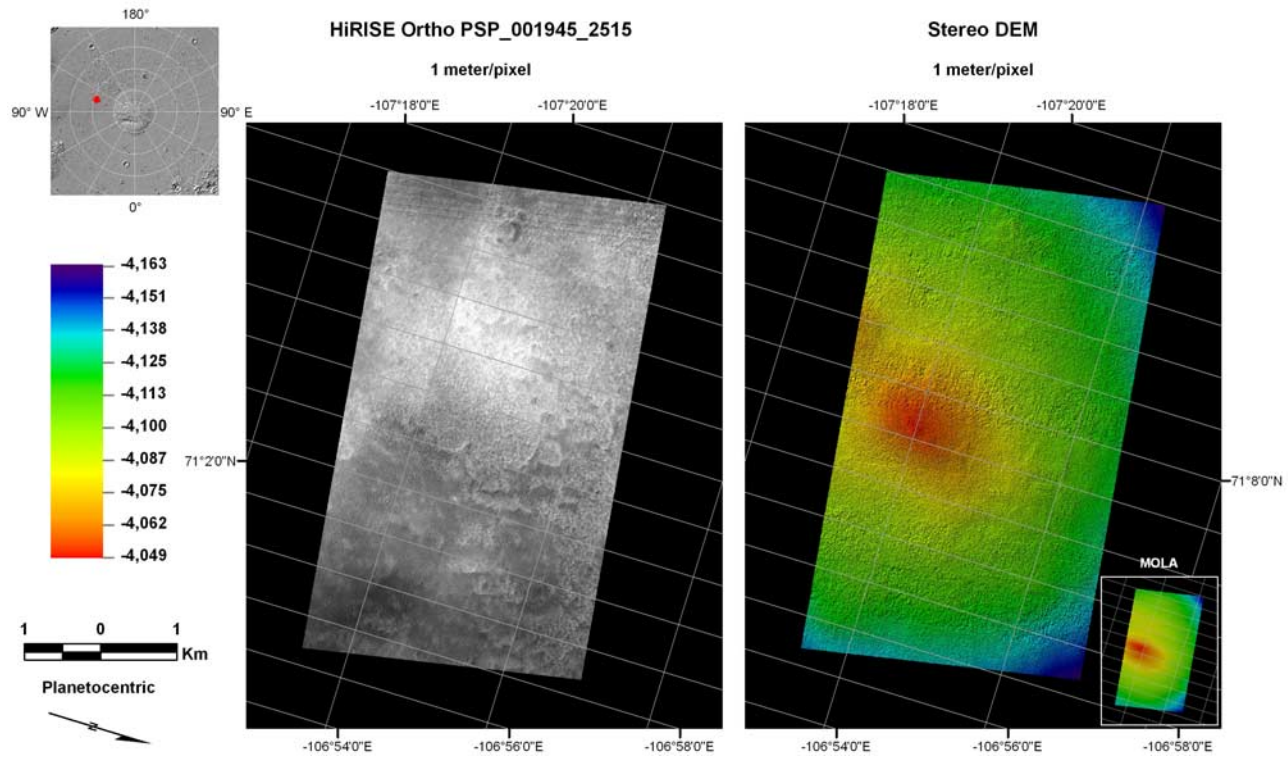


Figure 11. HiRISE stereopair PSP_001945_2515/PSP_002077_2515 in box 3, the third final candidate site. Portions of this DTM are of poor quality because of cloud obscuration in the second image of the pair (not shown). The broad maximum in elevation in the center of this region permitted the horizontal registration of the data to MOLA to be determined, on the basis of a preliminary, uncontrolled DTM. Presentation as in Figure 9.

tional slope, a slightly smaller ratio than was typical for MOC-derived slopes at 5-m baseline [Kirk *et al.*, 2003b]. The adirectional slope at the 99th percentile for box 3 is only 4.5° , which can be explained as the result of smoothing the artifact-filled DTM with a boxcar filter: most slopes occur at the edges of the filter box surrounding an erroneous DTM point, so are steep in either the line or the sample direction but not both. As a result, adirectional slopes are only slightly greater than the bidirectional slopes along the sample direction.

[48] Adjusting the relative positions of the CCD images before mosaicking reduces the discontinuities in the image data to less than a pixel, and thus limits the “cliffs” in the DTMs to amplitudes of less than about 1 m. These offsets vary along the image with a wavelength on the order of 2000 image lines, corresponding to spacecraft oscillations with a period on the order of 0.2 s. As shown in Figure 14, however, artifacts of this magnitude appear quite significant in comparison to the low relief of the candidate landing sites. Because the discontinuities involve an elevation change of as much as ~ 1 m across the 1-m space between adjacent DTM posts, the local slope can be quite steep, and it is appropriate to consider how the overall slope statistics are biased. The seams occur every 2000 image pixels across the image, or roughly every 600 DTM posts, so they should

only change the cumulative probability density function of slopes at the 99.8 percentile level and beyond. The RMS slope is biased by the presence of the seams, but not by an amount that is significant even in relation to the typical slopes. For example, we calculate a RMS bidirectional slope (east-west, or nearly perpendicular to the seam direction) of 2.15° for a 512×512 subarea of the box 1 DTM that contains no DTM seams and 2.32° for an area shifted slightly to include a seam. The fractional increase in RMS slopes would be larger for smoother surfaces and smaller for rougher ones; it is clear that this effect will not bias the RMS slopes enough make a safe site appear dangerous. The steep apparent slopes of the artifacts could cause simulated landings on or near them to fail. Whether such spurious failures occur frequently enough to influence the safety conclusions from Monte Carlo EDL simulations remains to be seen. If so, it may be necessary to exclude simulated landings that are too close to the artifacts from consideration.

3.6. Photoclinometry

[49] The results of the previous section are encouraging for the safety of the new candidate Phoenix landing sites. Slopes steeper than 16° would seem to be extremely rare at the 1-m grid spacing of the stereo DTMs. It should be noted, however, that the HiRISE images show patterned ground

Phoenix B8

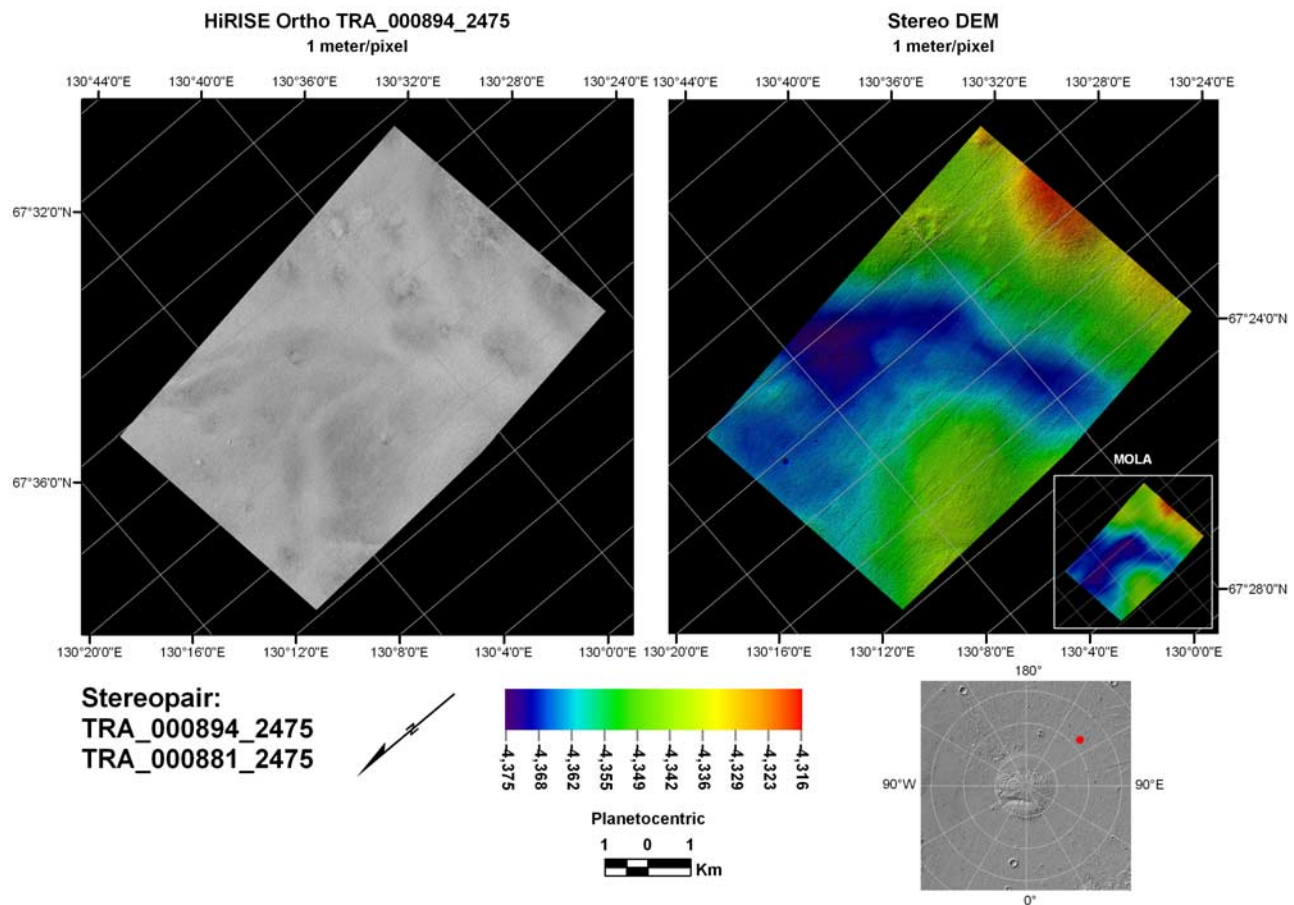


Figure 12. HiRISE stereopair TRA_000894_2475/TRA_000881_2475 in region B. This location was the leading candidate site until these and other early HiRISE images revealed large abundances of meter-scale rocks, forcing a search for safer sites. Although the rock density is higher here, the HiRISE DTM shows that surface slopes are comparable to those in the new sites in boxes 1 to 3. As for box 3, this data set has been controlled horizontally to MOLA, on the basis of the identification of unique correspondences between topographic features in the stereo and altimetric DTMs. Presentation as in Figure 9.

with polygons 10–20 m across and relatively narrow raised rims and interpolygon grooves only a few meters across at most. The latter are clearly not resolved in the 1 m post⁻¹ stereo DTMs (Figure 13). Thus, the stereo DTMs may systematically underestimate the true slopes over 1-m baselines. To estimate slopes over baselines down to a single pixel, we turn to two-dimensional photoclinometry, or shape-from-shading [Kirk, 1987; Kirk *et al.*, 2003a, 2003b]. One of the key problems with applying this technique to images of a body like Mars that has an atmosphere is that the contrast of surface features is diminished by atmospheric haze to a degree that varies unpredictably from image to image. Thus, an appropriate estimate of the surface-independent haze contribution to the image must be subtracted before PC will give quantitatively accurate results. Methods for estimating this haze level fall generally into two classes: those that rely only on the image data and those that make use of a priori topographic information as well. In the former category, haze estimates can be obtained by measuring the image radiance over a

shadowed area or a nonreflecting surface patch such as a lake (on Earth, and possibly on Titan, but not on Mars). In the latter category, one can either simulate a haze-free image from an a priori DTM and then compare it to the real image to determine how much haze is present or perform PC with various haze values and select the value that gives the best agreement between the a priori and PC DTM. In either case, success is dependent on having topographic features that are resolved in both the image and the a priori topographic data. The largest hummocks in the patterned ground of the Phoenix sites, which are 30 to 100 m across, can in many (though not all) cases be identified in both the real images and simulated images calculated from the DTMs (Figures 9–14). These features are only ~1 m high, only a few times the ~0.2-m estimated vertical precision of the stereo data; slopes on their flanks are no more than a few degrees. Excellent agreement between the stereo DTM and PC result is nevertheless obtained for features that can be seen in both data sets. The heights and slopes of individual hummocks agree at an accuracy of ~20%, leading us to conclude that

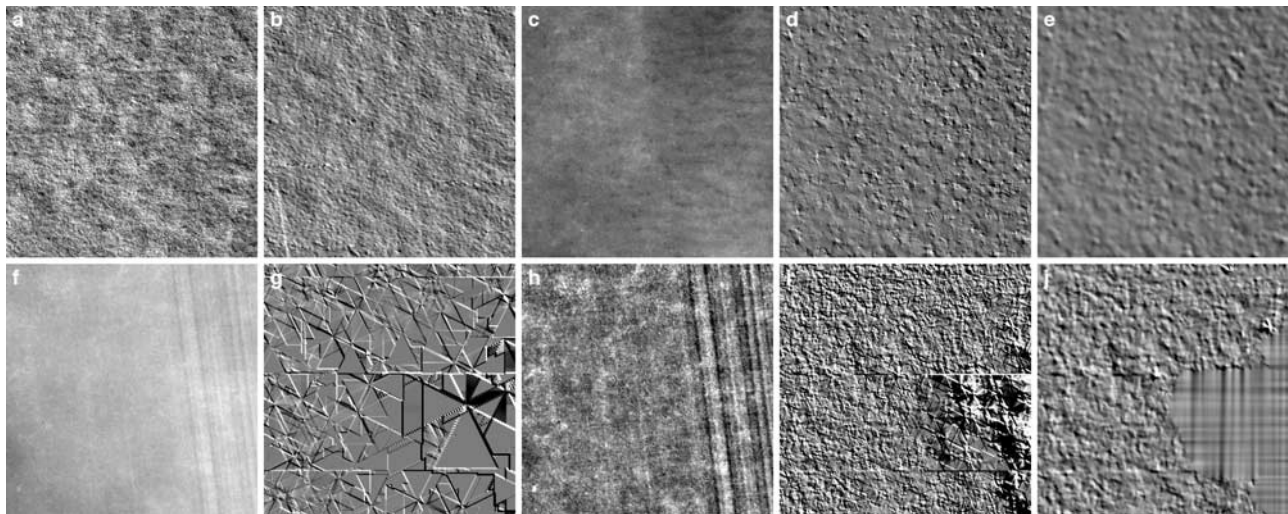


Figure 13. Examples of the variable quality of HiRISE images for the candidate Phoenix sites and the resulting variations in DTM quality. All areas shown are 400 m on a side. (a) Subarea of image PSP_001959_2485 in box 1. Both images in this box and in box 2 have good quality throughout. (b) Shaded relief from subarea of box 1 stereo DTM corresponding to Figure 13a. Note the correspondence of hummocks in Figures 13a and 13b. Minor artifacts are visible (including a detector seam at lower left) but the DTM quality is generally good, and no additional filtering was performed before slope statistics were calculated. (c) Subarea of image PSP_002077_2515 in box 3. Atmospheric opacity is better than average for this image but inferior to the other images used. (d) Shaded relief for area of raw DTM corresponding to Figure 13c. Note minor artifacts (bumps, pits, and polygonal features) caused by matching errors. (e) Shaded relief for same DTM area as Figure 13d, after smoothing with a 3×3 low-pass boxcar filter to suppress the artifacts. Fine-scale texture of the DTM is still dominated by artifacts not related to the surface features visible in Figure 13c, rendering the slope estimates from “good” areas of this smoothed DTM an upper limit. (f) Subarea of the box 3 image with below-average image quality as a result of localized cloud cover. Stretch is identical to Figure 13c. (g) Shaded relief corresponding to Figure 13f, from the unedited DTM. “Maltese cross” polygonal matching artifacts are severe, particularly at right where detector columns are poorly calibrated. (h) Image subarea corresponding to Figure 13f, after high-pass filtering and contrast enhancement in an attempt to bring out surface details. (i) Shaded relief from DTM based on matching high-pass-filtered images as in Figure 13h. Result contains a greater density of successfully matched points than Figure 13g, but is still dominated by artifacts. In areas of better image quality (like Figure 13c) the DTM from filtered images resembles the left side of this area, with more severe artifacts than the unfiltered version Figure 13d. (j) Final DTM of the same area, after editing in SOCET SET. Where the results from matching filtered images are better than those from the unfiltered images, they have been smoothed to further suppress the artifacts. Areas with severe matching artifacts even with the filtered images were outlined and replaced by interpolated data, as at right. Although this part of the DTM follows the overall surface as revealed by MOLA, very little information about surface detail remains. Areas of poor image quality like this were excluded from slope statistics for box 3, which were collected from areas where the unfiltered images yielded DTM quality similar to Figure 13e.

the overall calibration of PC from several such features is accurate to perhaps 10%.

[50] The images also contain numerous shadows associated with rocks. These shadows are typically 3 pixels across, with none larger than 5 pixels in their shorter dimension. Unfortunately, when we compared haze estimates based on the HiRISE stereo DTMs with those from direct measurement of shadows, we found a substantial disagreement. The best fit haze based on the amplitude of hummocks in the box 1 DTM is about 45% of the radiance for a level surface exposed to the sun (or, equivalently, of the average radiance over a region much larger than either shadows or hummocks). Typical shadows, which occupy about 0.1% of the image in the areas of highest rock density, have about 78% the radiance of a level surface. Only a few

isolated pixels (which are presumably influenced by noise) are as dark as 72%. Our initial PC DTM, produced with the 78% haze level set by typical shadows, was thus exaggerated by a factor of $(1 - 0.45)/(1 - 0.78) = 2.5$.

[51] Similar comparisons between shadow radiances and the haze level derived by fitting to the stereo DTM produced almost perfect agreement in a later stereopair (produced for HiRISE science team analysis) that contained relief of hundreds of meters and shadows tens to hundreds of pixels across. The apparently good haze estimates obtained from large shadows led us to hypothesize that the small (3–5 pixel) shadows of rocks are “diluted” by light from nearby illuminated areas that is scattered within the HiRISE optics. Figure 15 shows an estimate of the HiRISE optical point spread function (PSF) based on images of stars

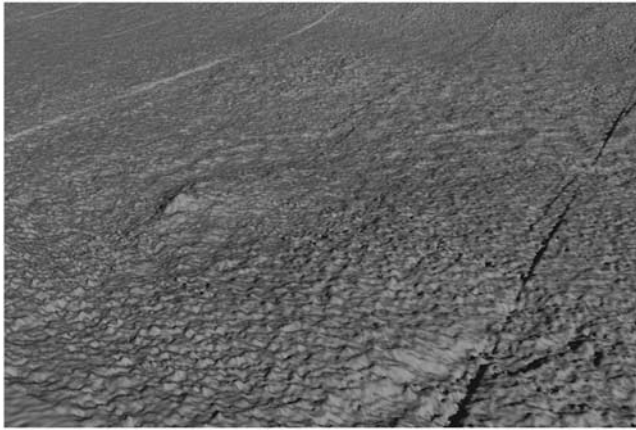


Figure 14. Perspective view (vertical exaggeration 4.5) of box 1 stereo DTM, showing discontinuities ≤ 1 m in amplitude caused by residual subpixel mismatches between CCD detectors.

obtained to support geometric calibration. The core is narrow (full width at half maximum 1.6 pixels) but integration of the area under the curve under the assumption of circular symmetry suggests that about half the apparent signal in any given pixel comes from points more than 3 pixels away. One might question whether this PSF measurement, obtained from star calibrations during cruise, applies to when Mars is being imaged. Additional blurring of the images might be caused by rapid “jitter” motions, broadening the PSF compared to what is shown in Figure 15. In fact, the stereo observations of Mars are obtained in “high-stability mode” with the motions of the main sources of jitter, the Mars Climate Sounder [McCleese *et al.*, 2007] and the solar arrays, paused. The spacecraft platform itself is believed to be more stable at the rotation rate needed for Mars imaging, for which it was primarily designed, than at the slower rotation rates used for star imaging. The fastest jitter motions revealed by the detector-to-detector offsets that give rise to discontinuities in the stereo DTMs (Figure 14) have a wavelength of ~ 2000 lines and an amplitude on the order of 1 pixel, leading to ~ 0.1 pixel of blur during 128 lines of TDI. Additional blur could be caused by very fast motions with periods less than the 0.01 s TDI period that would not be revealed by DTM artifacts, but the high-stability mode excludes the known sources of such vibrations. A final piece of empirical evidence that indicates that the images are not blurred by more than the 1.6 pixels of the PSF in Figure 15 comes from estimates of landing site rock abundances [Golombek *et al.*, 2008b]. Rock counts at the Viking landing sites are complete, when compared to ground truth from the landers, for diameters greater than about 1.5 m. Even in favorable cases, 3 to 5 pixels across a feature are needed to ensure that the feature is recognizable, so this result suggests that the true resolution of the HiRISE images is at most only slightly poorer than the pixel scale would suggest.

[52] We therefore investigated the effect on shadow radiances of deconvolving the optical PSF from the images. A pure inverse filter was implemented by dividing the Fourier transform of an image region by the transform of the optical PSF derived from the Stellar M data, then

performing the inverse Fourier transform [Castleman, 1996]. Figure 16 compares a portion of the box 1 image PSP_001959_2485 before and after such inverse filtering. Localized real features such as rocks and polygon boundaries have clearly been sharpened by the filter. Pixel-to-pixel fluctuations in the image have also been increased as a result of the filter amplifying both noise and real single-pixel features in the image. More sophisticated filtering techniques such as Weiner filtering could be used to suppress the highest spatial frequency fluctuations while sharpening broader features if desired, but on the basis of the appearance of images such as Figure 16b, we did not judge this to be necessary. The darkest few pixels in the filtered image areas (representing $\sim 0.0001\%$ of the area processed) had radiances very close to the haze level determined by calibration against the stereo DTM, but this seems likely to be a coincidence. Not only were these pixels darker than most neighboring shadow pixels, indicating that they were probably influenced by noise, they were invariably located near the edges of the filtered images where boundary effects from the filter are likely. More typical dark cores of shadows (about 0.1% of the rockiest areas) had on the order of 62% the level-surface radiance. Use of these deconvolved shadows to calibrate PC would thus result in overestimating the relief by a factor of $(1 - 0.45)/(1 - 0.62) = 1.4$, an improvement over the result for unfiltered images but still substantially in error. It is possible that deconvolution with an improved model of the HiRISE PSF that takes better account of the long tails that contribute most of the scattered light might yield more accurate radiances for small shadows. Even with the current PSF deconvolution, haze estimates from slightly larger shadows (perhaps on the order of 10 pixels) might be accurate enough to be useful. At present, we rely on stereo DTM data as the most reliable way of calibrating PC, but

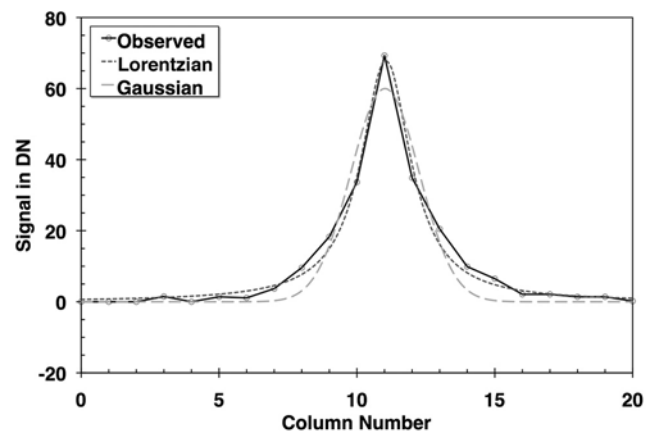


Figure 15. Central profile through HiRISE optical point spread function (PSF) as estimated from star images in Stellar M calibration sequence. Also shown are best fit Gaussian and Lorentzian models, which have width parameters of 1.24 and 0.77 pixels, respectively. The Gaussian fit is a poor compromise between a narrow central peak (full width at half maximum ~ 1.6 pixels) and long tails that are better described by the Lorentzian distribution. For this PSF, half the signal in a given pixel comes from features three or more pixels away.

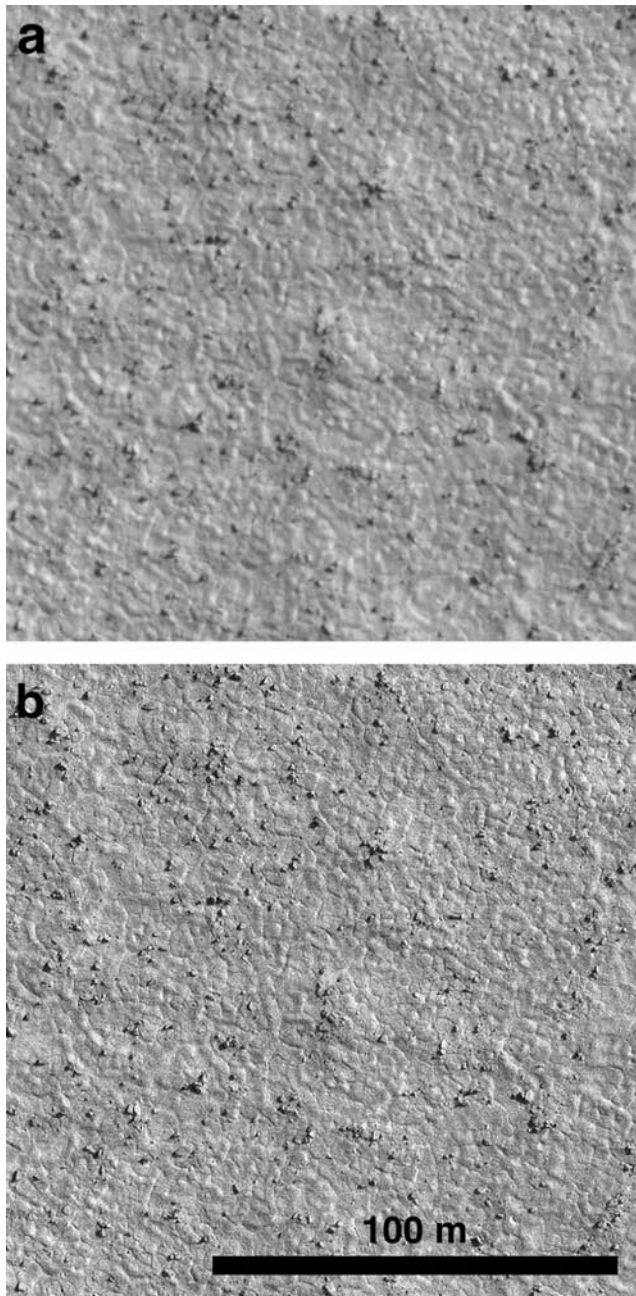


Figure 16. A small region (160 m across) within photogrammetry area a of HiRISE box 1 image PSP_001959_2485 (see Figure 17). (a) Unfiltered. (b) After inverse filtering to deconvolve point spread function estimated from star images. Both versions are identically contrast-stretched and are in raw camera geometry with north approximately at bottom.

will continue to compare the DTM-derived haze estimates with deconvolved shadow radiances to gain a better understanding of the circumstances under which the latter may be reliable. The advantage of being able to produce calibrated PC DTMs without the need for a stereo DTM is obvious: it would increase by roughly a factor of 10 the number of sites for which very high resolution topographic information could be derived from HiRISE images.

[53] We performed photogrammetry on a total of four subareas (designated a to d) of the box 1 image PSP_001959_2485 that were chosen to sample the full range of surface textures present (Figure 17). The broad hummocks present in subarea a were used to calibrate the results against the stereo DTM as described above, and the resulting haze level was used in processing the other areas also. Slopes computed from the initial PC DTMs, which were made from the orthorectified 8-bit images, showed a disappointing lack of resolution; these DTMs were essentially smooth at scales smaller than 1.5 m or about 5 pixels. The HiRISE optical PSF is the most obvious but not the only source of this smoothing. The images had also been smoothed by multiple resamplings (once in noproj and a second time during orthorectification), and the DTMs were resampled to orient them so that albedo-related artifacts could be filtered out [Kirk *et al.*, 2003b]. We therefore performed PC on PSF-deconvolved images in the original camera geometry and oversampled the DTMs to avoid smoothing during the filtering process. The resulting slope-baseline curves, which are included in Figure 2, show only a slight tendency to roll over at baselines smaller than 0.6 m (2 pixels), indicating that much of the loss of resolution seen in the preliminary results has been avoided. Single-pixel slopes were increased by 30–40%, but those at 1-m baseline by only 15–25% compared to the earlier results. Slopes for subarea a agree closely with those from the stereo DTM at baselines of 30–60 m, which is not surprising because the haze calibration was based on the large hummocks in this area. The other subareas are smoother at long baselines. All four areas have slopes at 1-m baseline that are comparable to but slightly greater than those obtained by stereoanalysis. A slope of 16° , which would be unsafe for Phoenix, is several times the RMS slopes shown in Figure 2 and Table 6 and thus would occur for only a tiny fraction of the area mapped.

4. Future Work

[54] The landing site mapping work described in the previous section was completed and products were delivered to the Phoenix Project in May 2007. On 1 June 2007, the box 1 site was officially selected as the final landing site. We are committed to providing additional support to the mission by extending the work reported here, to the extent that available data and resources permit. One possibility that was considered early on was exploiting additional MOC images, obtained near the end of the MGS mission, to provide 10 m post⁻¹ DTMs of a few more areas within the latitude zone of the landing site though probably not near the site itself. A more useful task is the production of additional HiRISE DTMs of the selected landing site from stereopairs acquired after conditions once again became favorable for imaging in the spring of 2008. In May 2008 we produced an additional DTM of some of the steepest terrain in the box 1 landing ellipse from images PSP_008143_2480 and PSP_008301_2480. Slope results from this DTM were used in the decision process for making final adjustments to the trajectory of the spacecraft. On 25 May 2008 the Phoenix spacecraft landed successfully, and images containing the lander and related hardware were obtained shortly thereafter. We have re-

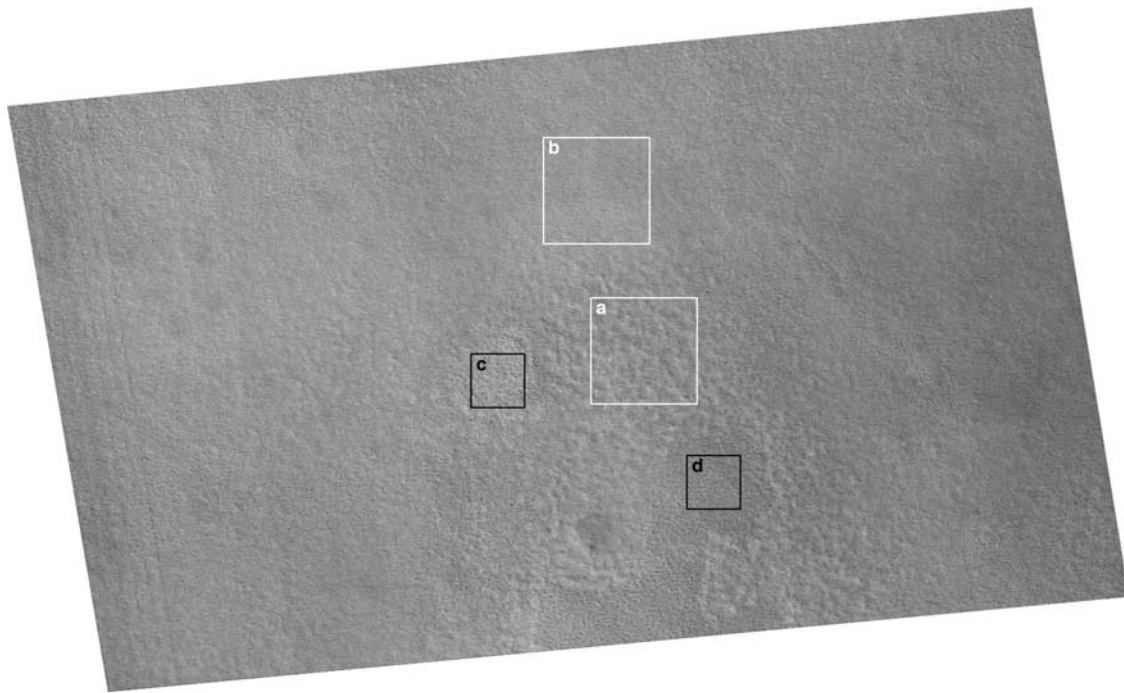


Figure 17. Orthorectified HiRISE box 1 image PSP_001959_2485 showing the location of subareas spanning the range of local geomorphology, selected for mapping by photoclinometry. (a) Large hummocks, low rock abundance. (b) Smooth, low rock abundance. (c) Intermediate roughness, high rock abundance. (d) Smooth, high rock abundance. Areas a and b are 2048 pixels square, and areas c and d are 1024 pixels square. Equirectangular projection with north at top.

cently completed a DTM of the landing site from images PSP_008591_2485 and PSP_008644_2485. We have also begun producing HiRISE DTMs of candidate landing sites for the 2009 Mars Science Laboratory Rover [Golombek *et al.*, 2008a].

[55] Immediately after completion of the Phoenix mapping reported here, we began to make DTMs in support of scientific investigations within the HiRISE team. Among the regions already identified as of greatest interest are young or potentially active features (gullies, high-latitude flow lobes and crevasses, polar “spiders” and geysers, polar layered terrain, and sublimation scallops in Hellas Planitia), stratigraphic sequences and contacts (layered deposits in Valles Marineris and craters, including Holden and Eberswalde deltas), tectonic features (faults in Candor Chasma), the freshest volcanic features (e.g., in Athabasca Valles), impact features (very fresh craters, possible secondaries), and past landing sites, where ground truth is available. Some of these areas contain very dramatic relief (especially in comparison to candidate landing sites), with local elevation differences in excess of 1000 m. Several such areas have already been mapped, but the volume of HiRISE stereo data being acquired (~1000 pairs planned for the one-Mars-year prime mission, of which roughly 500 have been completed as of this writing) would take us years if not decades to process. Improving and streamlining our photogrammetric processing will therefore remain one of our objectives indefinitely. We have also begun to train researchers (initially within the HiRISE team, though others are now following) who have purchased photogrammetric workstations with SOCET SET in the DTM production

procedures we have developed. Some of the specific aspects of photogrammetric processing that we are currently investigating are described in the following subsections.

4.1. Relative Control and Elimination of Jitter

[56] The severity of the jitter effects seen in MOC stereo-pairs, which commonly introduced obvious “washboard” distortions into the DTMs and could even prevent automated matching, led us to worry before the MRO mission that jitter could be a serious problem for stereoanalysis of HiRISE images. Fortunately, as noted in section 3.6, HiRISE stereo observations are usually obtained in high-stability mode with the main sources of spacecraft vibration temporarily stilled. For stereopairs obtained in this way, the main effects of unwanted motion are the near-constant misalignments of at most a few pixels between the adjacent CCDs, and smaller oscillations, usually 1 pixel or less in amplitude, with wavelengths of thousands of lines. Test images obtained while the Mars Climate Sounder (MCS) was operating confirmed that this instrument causes both severe (multipixel) image distortions and blur when it slews, and these effects are occasionally seen in images of interest for stereo mapping. For example, the pair PSP_001481_1875/PSP_002167_1880, covering Mojave crater that we processed for the HiRISE science team, was obtained partly in high-stability mode, but because of an error in the command sequence, the MCS resumed activity before the images were finished. The majority of the data in these ~80,000-line images are effectively undistorted; they were bundle-adjusted with low residuals and yielded a DTM without visible artifacts. The last ~15,000 lines, however,

had extremely high bundle adjustment residuals and contained visible internal distortions both parallel and perpendicular to the stereo baseline. Although we were able to process this portion of the stereopair, a high-quality DTM free of jitter-related artifacts could not be produced with our current procedures. Perhaps more importantly, as we process additional HiRISE stereopairs, we are encountering a small but significant fraction of images with jitter amplitudes greater than 1 pixel, and occasionally as much as 5 pixels peak-to-peak. Jitter less than about 2 pixels is tolerable, but more than 2 pixels of jitter results in reduced DTM quality, with bands of poor data (similar to Figures 13d or 13j even for images with good signal-to-noise ratio) where the along-track displacements of corresponding features put them so far from their expected positions that the matching algorithm fails to find them. This effect is in addition to the “washboard” ripples and discontinuities at CCD boundaries, which are proportional to the across-track jitter and thus have no well-defined threshold beyond which jitter effects go from acceptable to unacceptable. The dominant wavelength of the distortions tends to be somewhat longer, 4000–8000 lines, in these high-amplitude cases. We are currently developing techniques for correcting the jitter distortions in HiRISE images, which should both reduce the subpixel artifacts in the most stable images to negligible levels and allow us to produce high-quality DTMs from images with larger amounts of jitter distortion.

[57] The key to correcting jitter distortions is to obtain a model of the spacecraft-pointing history (i.e., an improved SPICE CK kernel) with significantly higher frequency sampling in time and greater precision. Processing of the image segments with *noproj* can then be done with this detailed kernel attributed to the real HiRISE camera, but with a smooth pointing history for the idealized camera in terms of which the output is defined. If the input CK accurately describes the jitter motions, their effects will be removed. The standard CK, which the MRO ACS generates by onboard synthesis of data from gyroscopes and star-tracker cameras, is sampled every 0.1 s (about 1000 image lines). This is insufficient to describe the fastest motions that could distort the images, which could have periods as short as 0.01 s or ~ 100 lines (any motions faster than the time delay and integration, which is 128 lines or less, will be integrated over, resulting in smear rather than distortion). In addition, the standard CK data are noisy because the pointing angles are coarsely quantized at a resolution of 0.035 mRad (35 pixels) during processing on board the spacecraft. Our tests show that using these standard kernels to project high-stability images actually increases the amplitude of jitter from ~ 1 pixel (for the raw, unprojected images) to ~ 10 pixels. We therefore smooth the information in the MRO CK files before using it for both standard and stereo processing. At present, this is done by fitting a quadratic polynomial to the data for each of the three rotation angles and using values from this fit. Considering that a quadratic curve can describe at most half a period of an oscillatory motion, this smoothing effectively eliminates any motions with periods shorter than twice the image duration, or about 2 to 16 s for images ranging from 10,000 to 80,000 lines.

[58] Fortunately, the images themselves provide the needed information about the high-frequency motions of the

spacecraft. Adjacent odd and even CCDs overlap by 48 pixels in the cross-track direction, and by correlating features that pass through these overlap regions we can estimate the changes in pointing over specific intervals of time and image lines. The along-track separation between the detector rows is ~ 600 lines (Figure 4), but the camera design deliberately includes slight departures from the average separation so that by comparing triplets of CCDs, we can estimate the pointing changes over shorter intervals [McEwen *et al.*, 2007]. For example, comparison of detectors 4, 5, and 6 provides constraints on the jitter over separations as small as 16 lines (Table 3). Overlaps between the red, blue-green, and infrared detectors in the center of the swath provide even more information about spacecraft motion over intervals of ~ 1200 lines.

[59] The software to match features in the CCD overlaps (ISIS programs *hijitreg* and *autoseed*) already exists. What is needed is software to produce improved CK files from this information. The design of such software potentially requires considerable care. If the information about rotation differences obtained from the feature matches were simply integrated over the time of imaging, the resulting CK would gradually diverge from the true pointing trajectory as random measurement errors accumulated. The problem should ideally be formulated as the optimal estimation of a new CK, given the various sources of information available (image matches, the standard CK, and unfiltered gyroscopic data sampled 200 times per second that are downlinked with each HiRISE image) and the uncertainties of these inputs. Given that the standard CK is not only coarsely quantized, but is produced from (and hence partly redundant with) the gyro data by a frequency-dependent filtering process [Lee *et al.*, 2003], weighting the inputs properly would be a challenge. Determining the most effective way to represent the jitter motions would also require experimentation.

[60] Our early results with HiRISE stereo processing suggested that it might not be necessary to solve this difficult general problem. The dominant motions, with wavelengths in the range of 2000–8000 pixels, can be modeled by a polynomial of modest order, provided the number of oscillations are small enough (i.e., for images of only a few tens of thousands of lines). We recently modified the ISIS 3 bundle adjustment program *jigsaw* to fit rotational (and trajectory, if desired) parameters with polynomials of arbitrary order, and so that images obtained simultaneously, such as those from the different HiRISE CCDs, can be modeled with a single set of polynomials as a function of time. The tendency of the tiepoint-based pointing solution to drift over time is corrected by merging a low-pass-filtered version of the original CK with a high-pass-filtered version of the *jigsaw* solution. Tests show that, with detector-to-detector ties from *hijitreg* as input, *jigsaw* can solve for a polynomial jitter model up to order 20, which suffices to fit no more than seven jitter oscillations, and thus to de-jitter images with 14,000 to perhaps as many as 50,000 lines. Modeling the jitter in longer images by this approach would require segmenting the images or replacing the polynomial representation (which becomes numerically unstable for higher orders) with an alternative such as orthogonal polynomials, splines, or a set of fixed or variable eigenfrequencies. A promising alternative approach has

recently been developed by HiRISE team members at the University of Arizona (S. Mattson and A. Boyd, written communications, 2008). In this method, the detector-to-detector ties are modeled by a Fourier series, from which a Fourier representation of the net motion of features in the focal plane can be derived analytically. Appropriate averaging of data from multiple detector pairs solves the problem that each individual pair is “blind” to certain specific frequencies of oscillation. We have implemented software to convert models of motion in the focal plane into C kernels (again, using a low-pass/high-pass filtering approach to merge the jitter solution with the low-frequency information in the standard CK) and shown that resampling the images based on the improved kernels eliminates most of the jitter. We expect that this methodology can be fully

automated and used to generate a jitter-corrected “precision CK” for the majority of HiRISE images in the near future.

4.2. DTM Production

[61] The small amount of editing required by most HiRISE DTMs came as a pleasant surprise, but we continue to look for ways to reduce the rate of DTM errors further and to improve the detail and fidelity of the results. Thus, we will continue to experiment with the parameters of the current SOCET SET stereomatching algorithm, ATE. More importantly, we are beginning to evaluate the “Next Generation Automatic Terrain Extraction” (NGATE) module that has recently been released by BAE Systems. The NGATE algorithm combines area-based and feature-based matching, matches all available combinations of overlapping imagery (in particular, within a single stereopair it matches both from the left to the right image and from the right to the left), and calculates all these match types at every image pixel. The multiple matching results for the same area are then compared to yield a consensus solution [Zhang, 2006; Zhang *et al.*, 2006]. For a wide variety of test cases including Mars Express HRSC imagery supplied by us [DeVenecia *et al.*, 2007], the result is both a decrease in the frequency of severe matching blunders and an improvement in DTM detail compared to ATE. Preliminary tests (Figure 18) suggest that similar improvements can be obtained with HiRISE data. We are optimistic that careful adjustment of the “strategy” parameters that control the NGATE algorithm will result in even better DTMs requiring less editing.

[62] We have previously noted the difficulty of validating HiRISE stereo DTM results, given the coarser resolution of all other sources of orbital remote sensing data. This resolution difference can be turned to our advantage, however, for purposes of evaluating the generic photogrammetric processing techniques that apply to multiple types of images and for quantifying the achievable DTM quality and resolution in relation to the resolution of the input images. Although our HiRISE DTMs are by no means perfect, their horizontal resolution and vertical precision are vanishingly small in relation to the errors that can be expected when we

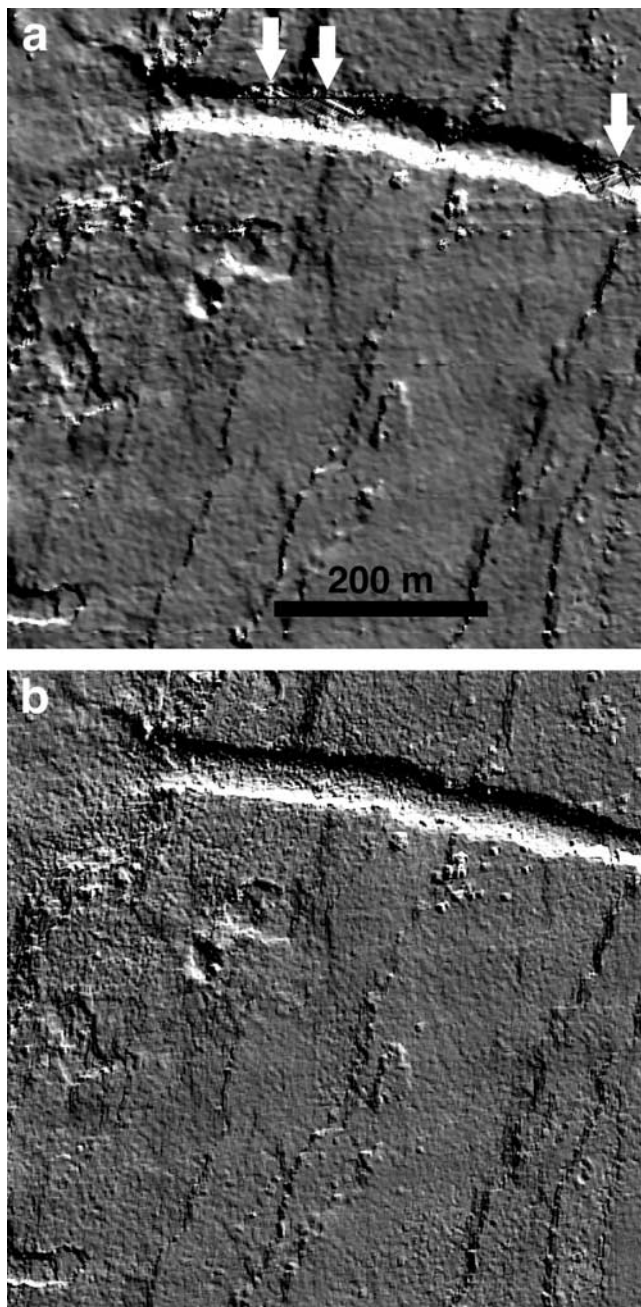


Figure 18. Evolving algorithms for automated image matching applied to HiRISE stereo. (a) A portion of a terrain shaded relief image made from a 1 m post-1 DTM of part of Athabasca Vallis based on images PSP_002661_1895 and PSP_003294_1895. Equirectangular projection, north at top. The SOCET SET Adaptive Automatic Terrain Extraction (AATE) algorithm [Zhang and Miller, 1997] was used. Note extensive artifacts with “Maltese cross” angular texture on the wall of the graben at top (arrows). Manual editing of such artifacts would be required for a finished DTM. (b) Corresponding area of a shaded relief image from a DTM produced with the SOCET SET Next Generation Automatic Terrain Extraction (NGATE) algorithm [Zhang, 2006]. “Maltese cross” artifacts have been eliminated, and the DTM as a whole appears sharper, though with some blockiness at high spatial frequencies. Adjustment of the NGATE algorithm parameters for a particular data type such as HiRISE is likely to yield further improvements in resolution and reduced error rate.

apply the same techniques to data sets such as Mars Express HRSC images, which have pixel scales nearly 2 orders of magnitude larger. Thus, coregistered HiRISE DTM data can in practice be used as a “truth” data set for evaluating the resolution and precision of HRSC DTMs in an absolute sense, complementing the largely relative comparisons of products generated by different approaches in the HRSC DTM comparison described by Heipke *et al.* [2007]. For example, we find that our SOCET SET DTM produced from ~ 25 m pixel⁻¹ nadir and ~ 50 m pixel⁻¹ stereo channel HRSC images of west Candor Chasma, which has a grid spacing of 75 m, has a true resolution closer to 200 m. Enhancement of the same DTM by photoclinometry yields a result comparable in its resolved details to a HiRISE DTM down-sampled to 75-m spacing [Kirk *et al.*, 2007]. Further such comparisons will guide our search to improve how we make use of the SOCET SET ATE and NGATE algorithms and will allow us to quantify the resolution and accuracy of our products better. To the extent that DTM properties scale with the image pixels, such quantitative estimates can also be extended to products from HiRISE and other instruments.

5. Conclusions

[63] The initial work reported here clearly demonstrates that the care taken in designing, building, and calibrating the HiRISE camera has paid off with an instrument that supports not merely qualitative photogeology, but quantitative topographic mapping at meter and submeter scales and quantitative change detection at subpixel scales. DTMs with a grid spacing of 1 m can be produced from HiRISE stereopairs by a straightforward extension of photogrammetric processing that was previously developed for other cameras. Such DTMs resolve features a few meters in horizontal extent, with a vertical precision of a few tenths of a meter, indicating that a stereo matching precision approaching 0.2 pixel has been achieved. Except in the most challenging circumstances of very steep and/or nearly featureless terrain, the abundance and severity of DTM artifacts requiring interactive editing are even less than predicted on the basis of the large size and high SNR of the images, and certainly much less than for any other planetary imagery with which we have worked. Photoclinometry offers the prospect of refining the stereo DTMs to the single-pixel level if the images are sharpened by PSF deconvolution. Where accurate haze intensities can be obtained by measuring moderate-sized shadows in the deconvolved images, this would also open up the prospect of obtaining high-resolution DTMs of areas of uniform albedo by photoclinometry even in the absence of stereo coverage. It is thus likely to be possible to sample the submeter-scale topography over many regions of Mars.

[64] Topographic mapping with HiRISE has revealed in particular that the short-baseline slopes as well as the geomorphology are similar at widely separated locations in the Phoenix latitude zone, both in the former candidate site in region B and in the final sites in regions A–D. Our best estimates of the RMS bidirectional slopes at 1-m baseline are in the range of 2–3°. The candidate Phoenix sites are thus smoother than in situ observations revealed the Viking 1 and Mars Pathfinder landing sites to be at meter scale. They are

also substantially smoother at scales of several to 10 m than the Viking 2 and MER A (Gusev plains) sites, though not than the MER B site in Meridiani Planum. The successful landing of Phoenix on 25 May 2008 and the very smooth plains revealed by the images from its Surface Stereo Imager have provided the final confirmation of our conclusions that rugged topography was not a significant hazard in the chosen landing site.

[65] **Acknowledgments.** The work reported here was supported by funding from the NASA Mars Reconnaissance Orbiter mission and the NASA Mars Critical Data Products program. We thank Matthew Golombek, Thomas Duxbury, and Kenneth Herkenhoff for their constructive reviews of this manuscript.

References

- Acton, C. H. (1999), SPICE products available to the planetary science community, *Lunar Planet. Sci.* [CD-ROM], XXX, abstract 1233.
- Anderson, J. A., S. C. Sides, D. L. Soltesz, T. L. Sucharski, and K. J. Becker (2004), Modernization of the integrated software for imagers and spectrometers, *Lunar Planet. Sci.* [CD-ROM], XXXIV, abstract 2039.
- Arvidson, R. E., et al. (2006), Overview of Mars Exploration Program 2007 Phoenix mission landing site selection, *Lunar Planet. Sci.* [CD-ROM], XXXVII, abstract 1328.
- Arvidson, R. E., et al. (2008), Mars Exploration Program 2007 Phoenix landing site selection and characteristics, *J. Geophys. Res.*, 113, E00A03, doi:10.1029/2007JE003021.
- Barge, L. M., and T. J. Parker (2006), Landing site map compilation and hazard assessment for Phoenix, *Lunar Planet. Sci.* [CD-ROM], XXXVII, abstract 2341.
- Batson, R. M., and E. M. Eliason (1991), Digital maps of Mars, *Photogram. Eng. Remote Sens.*, 61, 1499–1507.
- Becker, K. J., J. A. Anderson, S. C. Sides, E. A. Miller, E. M. Eliason, and L. P. Keszthelyi (2007), Processing HiRISE images using ISIS3, *Lunar Planet. Sci.* [CD-ROM], XXXVIII, abstract 1779.
- Boynton, W. V., D. M. Janes, M. J. Finch, and R. M. S. Williams (2006), Simultaneous determination of dry-layer thickness and sub-surface ice content in the polar regions of Mars: Implications for the Phoenix landing site selection, *Lunar Planet. Sci.* [CD-ROM], XXXVII, abstract 2376.
- Castleman, K. (1996), *Digital Image Processing*, 2nd ed., pp. 387–397, Prentice Hall, New York.
- DeVenecia, K., A. S. Walker, and B. Zhang (2007), New approaches to generating and processing high resolution elevation data with imagery, in *Photogrammetric Week '07*, edited by D. Fritsch, pp. 297–308, Wichmann, Heidelberg.
- Eliason, E. (1997), Production of digital image models using the ISIS system, *Lunar Planet. Sci.*, XXVIII, abstract 331.
- Gaddis, L., et al. (1997), An overview of the Integrated Software for Imaging Spectrometers (ISIS), *Lunar Planet. Sci.*, XXVIII, abstract 387.
- Gallagher, D., J. Bergstrom, J. Day, B. Martin, T. Reed, P. Spuhler, S. Streetman, and M. Tommeraaen (2005), Overview of the optical design and performance of the High Resolution Imaging Science Experiment (HiRISE), *Proc. SPIE Int. Soc. Opt. Eng.*, 5874, 198–207.
- Golombek, M. P., J. A. Grant, A. R. Vasavada, M. Watkins, E. Z. Noe Dobrea, J. L. Griffes, and T. Parker (2008a), Downselection of landing sites for the Mars Science Laboratory, *Lunar Planet. Sci.* [CD-ROM], XXXIX, abstract 2181.
- Golombek, M. P., et al. (2008b), Size-frequency distributions of rocks on the northern plains of Mars with special reference to Phoenix landing surfaces, *J. Geophys. Res.*, 113, E00A09, doi:10.1029/2007JE003065.
- Guinn, J., et al. (2006), The engineering behind Mars Exploration Program 2007 Phoenix mission landing site selection, *Lunar Planet. Sci.* [CD-ROM], XXXVII, abstract 2051.
- Hanisch, R. J., W. D. Pence, B. M. Schlesinger, A. Farris, E. W. Greisen, P. J. Teuben, R. W. Thompson, and A. Warnock (1999), *Definition of the Flexible Image Transport System (FITS)*, NOST 100-2.0, NASA/Sci. Off. of Standards and Technol., NASA Goddard Space Flight Cent., Greenbelt, Md. (Available at http://archive.stsci.edu/fits/fits_standard/)
- Heipke, C., et al. (2007), Evaluating planetary digital terrain models: The HRSC DTM test, *Planet. Space Sci.*, 55, 2173–2191, doi:10.1016/j.pss.2007.07.006.
- Hog, E., C. Fabricius, V. V. Makarov, S. Urbin, T. Corbin, G. Wycoff, U. Bastain, P. Schwendiek, and A. Wicenic (2000), The Tycho-2 catalog of the 2.5 million brightest stars, *Astron. Astrophys.*, 355, L27–L30. (Data available at <http://www.astro.ku.dk/~erik/Tycho-2/>)
- Howington-Kraus, E., R. L. Kirk, B. Redding, and L. A. Soderblom (1995), High-resolution topographic map of the Ares Tiu landing site from Vik-

- ing Orbiter data, in *Mars Pathfinder Landing Site Workshop II: Characteristics of the Ares Vallis Region and Fieldtrips in the Channeled Scabland*, Washington, LPI Tech. Rep. 95-01, part 2, pp. 38–39, Lunar and Planet. Inst., Houston, Tex.
- Kirk, R. L. (1987), A fast finite-element algorithm for two-dimensional photoclinoimetry, part III, Ph.D. thesis, pp. 165–258, Calif. Inst. of Technol., Pasadena.
- Kirk, R. L. (1993), Separation of topographic and intrinsic backscatter variations in bispocopic radar data: A “magic airbrush”, *Lunar Planet. Sci.*, *XXIV*, abstract 803.
- Kirk, R. L., J. M. Barrett, and L. A. Soderblom (2003a), Photoclinoimetry made simple. . .?, paper presented at ISPRS Working Group IV/9 Workshop “Advances in Planetary Mapping 2003”, Lunar and Planet. Inst., Houston, Tex., 22 March. (Available at http://astrogeology.usgs.gov/Projects/ISPRS/MEETINGS/Houston2003/abstracts/Kirk_isprs_mar03.pdf)
- Kirk, R. L., E. Howington-Kraus, B. Redding, D. Galuszka, T. M. Hare, B. A. Archinal, L. A. Soderblom, and J. M. Barrett (2003b), High-resolution topomapping of candidate MER landing sites with Mars Orbiter Camera narrow-angle images, *J. Geophys. Res.*, *108*(E12), 8088, doi:10.1029/2003JE002131.
- Kirk, R. L., E. Howington-Kraus, T. Hare, R. Soricone, K. Ross, L. Weller, M. Rosiek, B. Redding, D. Galuszka, and B. A. Archinal (2004), High-resolution topomapping of Mars: Life after MER site selection, *Lunar Planet. Sci.* [CD-ROM], *XXXV*, abstract 2046.
- Kirk, R. L., L. A. Soderblom, G. Cushing, and T. Titus (2005), Joint analysis of visible and infrared images: A “magic airbrush” for qualitative and quantitative topography, *Photogramm. Eng. Remote Sens.*, *71*(10), 1168–1178.
- Kirk, R. L., E. Howington-Kraus, D. Galuszka, B. Redding, and T. M. Hare (2006a), Topomapping of Mars with HRSC Images, ISIS, and a commercial stereo workstation [CD-ROM], *Int. Arch. Photogramm. Rem. Sens. Spatial Info. Sci.*, *XXXVII*(4), 293–298.
- Kirk, R. L., M. R. Rosiek, D. Galuszka, B. Redding, T. M. Hare, B. A. Archinal, and T. J. Parker (2006b), Topography of candidate Phoenix landing sites from MOC Images, *Lunar Planet. Sci.* [CD-ROM], *XXXVII*, abstract 2033.
- Kirk, R. L., et al. (2007), HiRISE: A new source of high-resolution topographic data for Mars, abstract 1119697, paper presented at European Mars Science and Exploration Conference, Eur. Space Agency, Noordwijk, Netherlands, 12–16 November.
- Lee, S. W., E. D. Skulsky, J. D. Chapel, D. Cwynar, R. Gehling, and A. Delamere (2003), Mars Reconnaissance Orbiter design approach for high-resolution surface imaging, AAS 03-067, in *Proceedings of the 26th Annual AAS Guidance and Control Conference*, NASA Jet Propul. Lab., Pasadena, Calif. (Available at <http://hdl.handle.net/2014/37230>)
- Li, R., et al. (2007a), Opportunity Rover localization and topographic mapping at the landing site of Meridiani Planum, Mars, *J. Geophys. Res.*, *112*, E02S90, doi:10.1029/2006JE002776.
- Li, R., et al. (2007b), Over three years of rover localization and topographic mapping for MER 2003 mission results, in *LPI Contribution 1353, Seventh International Conference on Mars*, Pasadena, Calif., abstract 3277.
- Liu, J., M. I. Richardson, and R. J. Wilson (2003), An assessment of the global, seasonal, and interannual spacecraft record of Martian climate in the thermal infrared, *J. Geophys. Res.*, *108*(E8), 5089, doi:10.1029/2002JE001921.
- Marlow, J. J., C. R. Klein, M. M. Martinez, B. S. McGrane, and M. P. Golombek (2006), Boulder hazard assessment of potential Phoenix landing sites, *Lunar Planet. Sci.* [CD-ROM], *XXXVII*, abstract 1094.
- McCleese, D. J., J. T. Schofield, F. W. Taylor, S. B. Calcutt, M. C. Foote, D. M. Kass, C. B. Leovy, D. A. Paige, P. L. Read, and R. W. Zurek (2007), Mars Climate Sounder: An investigation of thermal and water vapor structure, dust and condensate distributions in the atmosphere, and energy balance of the polar regions, *J. Geophys. Res.*, *112*, E05S06, doi:10.1029/2006JE002790.
- McEwen, A. S., et al. (2007), Mars Reconnaissance Orbiter’s High Resolution Imaging Science Experiment (HiRISE), *J. Geophys. Res.*, *112*, E05S02, doi:10.1029/2005JE002605.
- McGrane, B. S., and M. P. Golombek (2006), Geomorphology context and THEMIS appearance of boulder fields in Phoenix landing region B, *Lunar Planet. Sci.* [CD-ROM], *XXXVII*, abstract 1541.
- Mellon, M. T., W. V. Boynton, W. C. Feldman, R. E. Arvidson, T. N. Titus, J. L. Bandfield, N. E. Putzig, and H. G. Sizemore (2008), A prelanding assessment of the ice table depth and ground ice characteristics in Martian permafrost at the Phoenix landing site, *J. Geophys. Res.*, doi:10.1029/2007JE003067, in press.
- Miller, S. B., and A. S. Walker (1993), Further developments of Leica digital photogrammetric systems by Helava, *ACSM/ASPRS Annu. Conv. Exposition Tech. Pap.* 3, 256–263.
- Miller, S. B., and A. S. Walker (1995), Die Entwicklung der digitalen photogrammetrischen Systeme von Leica und Helava, *Z. Photogramm. Fernerkundung*, *63*(1), 4–16.
- Seelos, K. D., R. E. Arvidson, T. Parker, M. Golombek, L. Tamppari, and P. Smith (2006), Geomorphology and terrain characterization for the 2007 Phoenix mission landing sites in the northern plains of Mars [CD-ROM], *Lunar Planet. Sci.*, *XXXVII*, abstract 2166.
- Seelos, K. D., et al. (2008), Geomorphologic and mineralogic characterization of the northern plains of Mars at the Phoenix Mission candidate landing sites, *J. Geophys. Res.*, *113*, E00A13, doi:10.1029/2008JE003088.
- Smith, D. E., et al. (2001), Mars Orbiter Laser Altimeter: Experiment summary after the first year of global mapping of Mars, *J. Geophys. Res.*, *106*, 23,689–23,722, doi:10.1029/2000JE001364.
- Smith, P. H., et al. (2004), The Phoenix mission to Mars, *Lunar Planet. Sci.* [CD-ROM], *XXXV*, abstract 2050.
- Smith, P. H., et al. (2006), Science considerations driving the choice of the Phoenix mission landing site, *Lunar Planet. Sci.* [CD-ROM], *XXXVII*, abstract 1910.
- Smith, P. H., L. K. Tamppari, R. E. Arvidson, W. V. Boynton, and the Phoenix Science Team (2007), Phoenix landing site selection update, *Lunar Planet. Sci.* [CD-ROM], *XXXVIII*, abstract 1176.
- Smith, P. H., et al. (2008), Introduction to special section on the Phoenix Mission: Landing Site Characterization Experiments, Mission Overviews, and Expected Science, *J. Geophys. Res.*, *113*, E00A18, doi:10.1029/2008JE003083.
- Spiegel, M., R. Schmidt, U. Stilla, A. Baumgartner, G. Neukum, and the HRSC Co-Investigator Team (2005), Registering HRSC imagery of the Mars Express Mission to Mars Observer Laser Altimeter Data, *Lunar Planet. Sci.* [CD-ROM], *XXXVI*, abstract 1761.
- Squyres, S. W., et al. (2006), Overview of the Opportunity Mars Exploration Rover mission to Meridiani Planum: Eagle crater to Purgatory Riple, *J. Geophys. Res.*, *111*, E12S12, doi:10.1029/2006JE002771.
- Sullivan, R., J. Grotzinger, A. Knoll, M. Golombek, B. Joliff, S. Squyres, and C. Weitz (2007), Aeolian geomorphology with MER Opportunity at Meridiani Planum, Mars, *Lunar Planet. Sci.* [CD-ROM], *XXXVIII*, abstract 2048.
- Tanaka, K. L. (1997), Sedimentary history and mass flow structures of Chryse and Acidalia Planitia, Mars, *J. Geophys. Res.*, *102*, 4131–4149, doi:10.1029/96JE02862.
- Torson, J., and K. Becker (1997), ISIS: A software architecture for processing planetary images, *Lunar Planet. Sci.*, *XXVIII*, abstract 1443.
- U.S. Geological Survey (Comp.) (1991), *Mission to Mars: Digital Topographic Map, USA NASA PDS VO2007* [CD-ROM], U.S. Geol. Surv., Reston, Va.
- Vosselman, G., N. Sester, and H. Mayer (2004), Basic computer vision techniques, in *Manual of Photogrammetry*, 5th ed., edited by J. C. McGlone, p. 472, Am. Soc. of Photogramm. and Remote Sens., Bethesda, Md.
- Wells, D. C., E. W. Greinsen, and R. H. Harten (1981), FITS: A Flexible Image Transport System, *Astron. Astrophys.*, *44*, Suppl., 363–370.
- Wolf, P. (1983), *Elements of Photogrammetry*, 2nd ed., 628 pp., McGraw Hill, Boston, Mass.
- Zhang, B. (2006), Towards a higher level of automation in softcopy photogrammetry: NGATE and LIDAR processing in SOCET SET[®], paper presented at GeoCue Corporation 2nd Annual Technical Exchange Conference, Nashville, Tenn., 26–27 September.
- Zhang, B., and S. Miller (1997), Adaptive automatic terrain extraction, *Proc. SPIE Int. Soc. Opt. Eng.*, *3072*, 27–36.
- Zhang, B., S. Miller, K. DeVenecia, and S. Walker (2006), Automatic terrain extraction using multiple image pair and back matching, paper presented at ASPRS 2006 Annual Conference, Am. Soc. of Photogramm. and Remote Sens., Reno, Nevada, 1–5 May.

J. A. Anderson, B. A. Archinal, K. J. Becker, D. A. Cook, D. M. Galuszka, P. E. Geissler, T. M. Hare, I. M. Holmberg, E. Howington-Kraus, L. P. Keszthelyi, R. L. Kirk, B. L. Redding, and M. R. Rosiek, U.S. Geological Survey, Astrogeology Program, 2255 N. Gemini Drive, Flagstaff, AZ 86001, USA. (rkirk@usgs.gov)

J. D. Chapel, Lockheed Martin Space Systems, 12257 S. Wadsworth Boulevard, Denver, CO 80125, USA.

W. A. Delamere, Delamere Support Services, 2740 4th Street, Boulder, CO 80304, USA.

E. M. Eliason, R. King, and A. S. McEwen, Lunar and Planetary Laboratory, University of Arizona, Tucson, AZ 85721, USA.

D. Gallagher, CDM-Optics, 4001 Discovery Drive, Suite 130, Boulder, CO 80303, USA.